TIM

Acquisition and Reconstruction Techniques for B_1^+ Mapping Integrating Motion Compensation for Cardiac Magnetic Resonance Imaging

Teresa Rincón Domínguez

Vollständiger Abdruck der von der Fakultät für Informatik der Technischen Universität München zur Erlangung des akademischen Grades eines

Doktors der Naturwissenschaften (Dr. rer. nat.)

genehmigten Dissertation.

Vorsitzender:

Prof. Dr. Björn Menze

Prüfende der Dissertation:

1. Prof. Dr.-Ing. Darius Burschka
2. Priv.-Doz. Dr. Marion I. Menzel

Die Dissertation wurde am 27.06.2018 bei der Technischen Universität München eingereicht und durch die Fakultät für Informatik am 30.10.2018 angenommen.

ABSTRACT

Cardiovascular magnetic resonance (CMR) imaging is a powerful tool, which allows for the non-invasive assessment of tissues, and myocardial structure and function. CMR provides fundamental information for clinical diagnosis, treatment and management of cardiovascular diseases without exposure to ionizing radiation. However, field inhomogeneities caused by interactions between the radiofrequency (RF) field and the patient's anatomy can lead to artifacts and contrast variations in CMR images. Consequently, the overall image quality is degraded and thereby the diagnostic value of the images might be compromised, especially at high field strengths (≥ 3.0T). Furthermore, this problem is especially important in the context of quantitative MRI. Field inhomogeneities may hamper the measurement of tissue parameters, which are used to distinguish between lesions and healthy tissues.

This thesis presents a B_1^+ (RF transmit field) mapping technique that allows for the investigation of spatial homogeneity of the transmitted radiofrequency field in the myocardium at 3.0T. To this end, the presented work adapts the Dual Refocusing Echo Acquisition Mode (DREAM) sequence, currently one of the fastest sequences to measure both B_0 and B_1^+ in non-moving organs, in three aspects relevant for cardiac applications: 1) ECG-triggering, 2) a multi-snapshot undersampling scheme, which relies on the Golden Ratio to accelerate the acquisition, and 3) motion-compensation based on low-resolution images acquired in each snapshot.

The proposed technique is compared to the Bloch-Siegert shift method, validated against the standard DREAM sequence and tested in healthy volunteers. Resulting B_1^+ maps are analyzed

for six standard regions of interest within the myocardium. Consistency between free breathing and breath-hold values was found, which demonstrates the motion robustness of this method with good repeatability. Remaining limitations regarding flow sensitivity and ECG detection could be addressed in future work.

In summary, an efficient free-breathing and motion-robust B_1^+ mapping method with high spatial resolution in a reduced scan time per trigger is presented, implemented and evaluated in this thesis. The free-breathing characteristic of the proposed method can be particularly important to determine RF shim components for multi-channel systems, currently limited to two for a single breath-hold. Nevertheless, an accurate characterization of the B_1^+ field is also required in numerous MR applications. The presented approach can therefore be incorporated in the form of a calibration scan at the beginning of any MR examination. Moreover, it can be used to estimate the local specific absorption rate (SAR) distribution, which describes the RF deposition on the patient´s tissue and thus is essential for its safety. Additionally, it can be used in image processing to derive quantitative tissue parameters.

ZUSAMMENFASSUNG

D ie Kardiovaskuläre Magnetresonanztomographie (MRT) ist eine vielseitige diagnostische Modalität zur nicht-invasiven Beurteilung von Funktion und Textur myokardialer Strukturen. Sie liefert grundlegende Informationen über die klinische Diagnose, erfolgreiche Behandlung und das Monitoring kardiovaskulärer Krankheiten, ohne den Patienten dabei ionisierender Strahlung auszusetzen. Allerdings können Feldinhomogenitäten, verursacht durch Wechselwirkungen zwischen dem Hochfrequenz (HF) Feld und der Anatomie des Patienten, zu Bildartefakten und Schwankungen im Kontrast führen. Als Konsequenz wird dadurch die Bildqualität beeinträchtigt und dabei der diagnostische Wert der Untersuchung, insbesondere bei hohen Feldstärken ($\geq$3.0T), herabgesetzt. Des Weiteren ist dies besonders wichtig im Hinblick auf die quantitative MRT. Inhomogenitäten des Feldes können die Messung der Gewebeparameter, aufgrund derer zwischen Läsionen und gesundem Gewebe unterschieden wird, negativ beeinflussen.

In dieser Arbeit wird eine B_1^+ (HF Anregungsfeld) Bildgebungsmethode vorgestellt, welche es erlaubt, die räumliche Homogenität des übertragenen HF Feldes im Myokard bei 3.0T zu untersuchen. In der vorgestellten Arbeit wurde die 'Dual Refocusing Echo Acquisition Mode (DREAM)' Sequenz, derzeit eine der schnellsten Sequenzen um sowohl B_0 als auch B_1^+ in statischen Organen zu messen, angepasst. Für die Anwendung am Herzen wurde sie in drei Aspekten erweitert, nachfolgend um: 1) einen EKG-Trigger, 2) eine sich wiederholende unterabgetastete Momentaufnahme, basierend auf dem Goldenen Schnitt, um die Aufnahme zu beschleunigen, und 3) einer Bewegungskompensierung anhand eines niedrig aufgelösten Bildes, aufgenommen während jeder Momentaufnahme.

Die vorgeschlagene Methode wurde mit der der Bloch-Siegert Verschiebung verglichen, anhand der Standard-DREAM Sequenz validiert und in einer Studie mit gesunden Probanden getestet. Resultierende B_1^+ Karten wurden anhand von sechs standardisierten 'regions of interest' innerhalb des Myokardiums analysiert. Der Vergleich zwischen frei geatmeter Aufnahme und unter Atemstopp ergab übereinstimmende Werte, wodurch die Robustheit der Methode gegenüber Bewegung mit hoher Reproduzierbarkeit gezeigt werden konnte. Grundsätzliche Limitierungen bezüglich Flusssensitivität und EKG-Triggering könnten in zukünftigen Arbeiten behandelt werden.

Zusammenfassend wurde in dieser Arbeit eine effiziente, bewegungsinsensitive B_1^+ Bildgebungsmethode mit hoher räumlicher Auflösung bei reduzierter Aufnahmezeit pro Trigger unter freier Atmung vorgestellt, implementiert und evaluiert. Eine genaue Bestimmung des B_1^+ Feldes ist für eine Vielzahl von Anwendungen im Bereich des MRT, wie zum Beispiel Systemkalibrierung und HF 'shimming', Bildverarbeitung zur Bestimmung quantitativer Gewebeparameter, sowie zur Abschätzung der lokalen spezifischen Absorptionsrate (SAR), nötig. Die Tatsache, dass in der vorgeschlagenen Methode Daten unter freier Atmung akquiriert werden, könnte sie insbesondere für die Bestimmung der magnetischen Ausgleichsfelder ('shim') in Mehrkanalsystemen interessant machen, welche derzeit auf zwei Kanäle während eines einzelnen Atemstopps beschränkt sind. Sie könnte in Form eines Kalibrierungsscans zu Beginn der MR Untersuchung eingefügt werden. Darüber hinaus kann sie benutzt werden, um die Verteilung der lokalen spezifischen Absorptionsrate (SAR) abzuschätzen, die die HF Absorption im Gewebe des Patienten beschreibt, und daher für dessen Sicherheit essentiell ist. Zusätzlich kann sie in der Bildauswertung verwendet werden um quantitative Gewebeparameter zu bestimmen.

AKNOWLEDGEMENTS

CONTENTS

INTRODUCTION TO MRI

Magnetic Resonance Imaging (MRI) is a non-invasive imaging modality that enables the in vivo study of the structures and functions of biological systems. The fundamental principle that makes MRI possible is the phenomenon of Nuclear Magnetic Resonance (NMR). The NMR effect in solids and liquids was first described by Bloch [1] and Purcell [2] independently in 1946. In 1966, Ernst advanced this technology to a new level by introducing pulsed NMR and the Fourier transform as a method to understand data acquisition and image reconstruction. Since then, NMR spectroscopy has become one of the most important techniques to study the composition of chemical compounds.

The potential of NMR as a medical diagnostic tool was introduced in 1971 by Damadian [3]. He analyzed a wide range of tissues in rats and found differences in the response signals between tumor and healthy tissues. However, the fundamental development that led to the birth of MRI was in 1973 when Lauterbur [4] and Mansfield [5] presented methods to perform spatially resolved NMR experiments by employing position dependent magnetic fields. Few years later, in 1977, Mansfield and Maudsley [6] refined the method, producing the first image of a body part, a crossed-section of a finger.

During the last four decades, MRI has developed rapidly through continued efforts to improve the examination efficiency and image quality. Accelerating the imaging process has been one

of the priorities for the MR research community. The early discoveries of fast imaging techniques such as Fast Low Angle Shot (FLASH) [7] or echo-planar Imaging (EPI) [8] were widespread in clinical systems quickly. After that, the so-called parallel imaging approach, based on the encoding effect of the receiver coils, yielded to speed factors proportional to the number of additional coils incorporated into the scanner. Alternatively, compressed sensing enabled reconstruction of images with less acquired data. Recently, MR fingerprinting (MRF) [9] emerged as a promising technique based on a new data acquisition approach. MRF images are built on a small fraction of the scanner data matched to databases of known tissue patterns using advanced computation.

Nevertheless, these advanced techniques require calibration and compensation mechanisms to subdue different system imperfections such as field inhomogeneities or motion artifacts, considering that such artifacts may lead to misinterpretations in the images and a subsequent loss in diagnostic quality.

MRI is now an established modality in clinical diagnostics as well as in medical, biological, chemical, and physical research. The great strength of MRI is its remarkable flexibility. Modern MR scanners are meticulously engineered to control radiofrequency pulses and magnetic gradients to create different contrast possibilities which provide critical information in clinical settings. Compared to x-ray computed tomography (CT) methods, MRI distinguishes itself for its ability to visualize soft tissue with exquisite anatomical detail without relying on harmful ionizing radiation. Additionally, radioactive markers are unnecessary unlike Positron Emission Tomography (PET) or Single Photon Emission Computed Tomography (SPECT).

4

CHAPTER 1

Fundamental concepts

1.1. Overview of an MRI Examination

I N the following, the key components of hardware and software that allow for the creation of an MRI scan are outlined. At first, a general overview of the employed hardware is given. Then, most relevant components are discussed in more detail. Finally, the scanning process including pulse sequences is introduced to provide a general understanding of acquisition and reconstruction techniques in MRI.

1.1.1. MRI System Hardware

In a clinical setting, the MRI system is typically distributed between three rooms: the magnet room, the technical room, and the control room. The MRI scanner itself is located in the magnet room. In order to avoid hazardous situations that may hurt the patient or harm the scanning system only non-ferromagnetic items can be used for any setup in the scanner room. The technical room contains supporting electronics to control the magnet operation, e.g. power supply, cooling system and cabinets with the amplifiers for the gradient and RF systems. The

operator's console is the interface between the MR scanner and the technician and it is located in the control room. There, technicians can select appropriate scan acquisition parameters and view or post-process MR images.

The MR system hardware consists of:

- Magnet that produces a strong, constant magnetic field;
- Magnetic field gradient system (coils and amplifiers), which localize the MR signals;
- Radiofrequency transmit and receive coils, which excite and detect the MR signal;
- Computer system for scanner control, image display processing and archiving;
- Patient support table and positioning aids;
- Physiological monitoring equipment to examine patient's ECG and respiratory cycle.
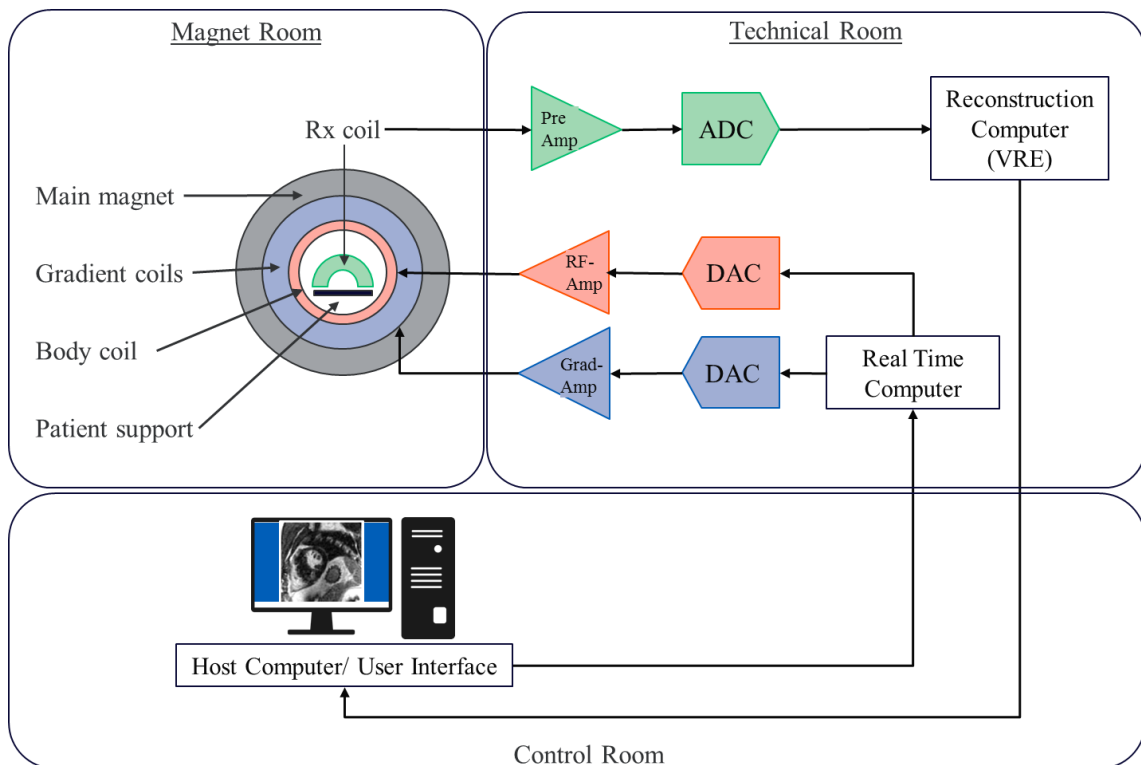
Figure 1.1: *Basic hardware components of an MR system. DAC and ADC denote digital-to-analogue converter and analogue-to-digital converter, respectively.*

The main magnet

A large cylindrical tubed magnet generates a strong, constant magnetic field (B_0) which is always present, even when the scanner is not imaging. In clinical scanners this is a superconducting coil cooled with liquid helium. The field strength ranges from 1.5T to 3T in most of the MRI systems for clinical use. Current state-of-the-art technology is pushing this upper limit to 7T and higher field strength in research systems, which is approximately 140,000 times the Earth's magnetic field.

One of the main magnet characteristics is its homogeneity, which describes the quality or uniformity of the magnetic field. This is crucial in order to ensure uniform signal over the field of view, to generate images with high signal-to-noise-ratio (SNR) and to avoid image distortions. After the manufacturing process, the magnetic field is non-uniform due to design constraints. However, homogeneity is adjusted either by active shim coils producing corrective fields, or passively, by placing small ferromagnetic plates along the field direction. The MR system used during the experiments of this thesis provides a field with a homogeneity of <4 ppm over a 50cm diameter of spherical volume. This means that no two points within $\pm\,25$ cm of the magnet isocenter differ in magnetic field strength by more than four parts in a million, or by no more than $3 \cdot 10^{-6}$ T.

The gradient system

The localization of the MR signal in the body of the patient is accomplished by generating spatial variations in magnetic field strength across the targeted volume of interest. The gradient fields are produced by a set of three separate gradient coil layers which are incorporated into the bore of the magnet. These coils alter the magnetic field strength linearly along the orthogonal x-, y-, and z-axes.

In order to generate these spatial variations, electrical currents of the gradient system are switched on and off during imaging. Typically, these gradients have a trapezoidal type

response as shown in figure 1.2. Gradient performance is defined in terms of the peak gradient strength (44mT/m) and the slew rate (200T/m/s). As the gradient magnetic fields cannot be switched on instantaneously, the slew rate is defined as the peak gradient field force divided by the rise time. The maximum slew rate is a decisive performance parameter of the scanner. With higher slew rates, the gradient fields can be switched quicker thereby reducing the duration of the image formation. Thus, faster scanning is performed with potentially higher spatial resolution.
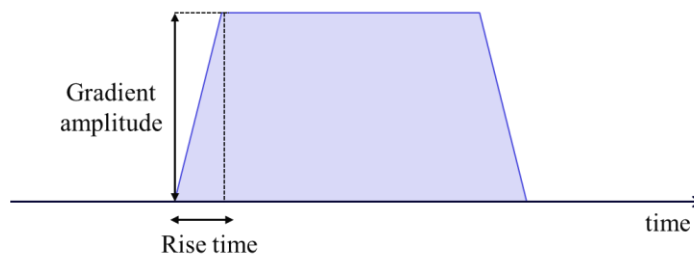
Figure 1.2: Key gradient specifications. Gradient pulses in conventional pulse sequences are trapezoidal in shape with an initial ramp, followed by a flat plateau and a final descent at the respective slew rate.

The radiofrequency (RF) system

The RF system comprises of a transmitter path (Tx), the transmitting coil and a receiver path (Rx), the receive coil. Tx coils are used for excitation of the nuclei within the patient's tissue. The function of a Rx coil is to detect the MR signal with maximal signal to noise ratio.

The body coil can act as both, transmit and receive coil. In the transmit mode, the actual pulse shape and bandwidth of the excitation pulse are set by the pulse generator i.e. the real-time computer. Thus, a DAC converts the RF signal into an analog waveform, which is conveyed to the transmit coil via the RF amplifier. In the receive mode, the detected signal has to be amplified again by a preamplifier to enhance the signal before it is further processed. The RF amplifier output rating is typically about 30 kW in body mode and 4 kW in head mode.

Since this coil is large, it has a very uniform transmission field, but this also means that it is not especially sensitive if used as a Rx coil. In cardiac examinations, the body coil is used as Tx only with a special coil used as Rx coil. Other specific coils, e.g. a head coil, may also be used for transmission. In this case less power is required to flip the magnetization. Excitation uniformity might be compromised too.
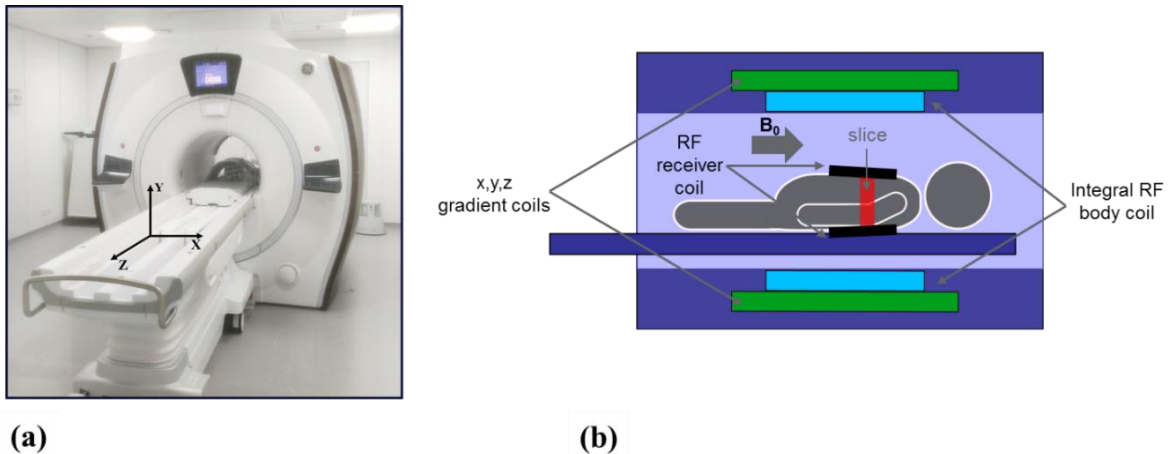
Figure 1.3: a) GE 3.0T 750w MRI scanner and conventional coordinate system used to define the main orientation axis of the scanner. b) Schematic drawing of a whole-body MRI scanner with dedicated cardiac receiver coils.

The computer system

There are at least three independent computers in an MRI system to control and coordinate all the processes involved in data acquisition and reconstruction. A typical MRI system has a host computer on which the technician prescribes the scan in terms of the pulse sequence protocol, its timing and various geometry factors. These parameters are converted into commands that are transferred to the real-time computer, which controls the scanner hardware and ensures that the gradients, RF pulses and data acquisition are all properly synchronized. Its instruction memory can be updated every four microseconds. The third system, known as the volume reconstruction engine (VRE), is used for reconstruction of images based on the raw MR data. Finally, the host computer manages the image display, processing and archiving.

1.1.2. The Scanning Process

In clinical practice, the duration of an MRI examination ranges from 10 to 60 minutes and consists of several scanning protocols. Not all the scans conducted during the MRI examination are explicitly related to diagnostic imaging. Prior to the actual image acquisition, calibration and localization scans are conducted as detailed in the following.

Prescan

Typically, each imaging sequence is preceded by a prescan or calibration phase, in which the characteristics of the transmitter and receiver are optimized depending on the setup, coil configuration and weight of the patient. The first step involves determining the exact resonant i.e. Larmor frequency of the targeted hydrogen protons (see section 1.2.1). Accordingly, the necessary slice offsets can be calculated. In the second step, the necessary RF power, required to generate a known flip angle, is determined by adjusting the output of the RF power amplifier. Finally, the receiver gain is adjusted so that the signal coming back from the patient matches the input voltage range of the ADC.

Imaging Pulse Sequences

An MRI pulse sequence consists of a sequential replication of RF and gradient pulses that controls the excitation and read-out of the signal which affects the image characteristics. Pulse sequences are defined as the software that controls the required hardware to apply the different encoding mechanisms.

In figure 1.4, the diagram of the Gradient Echo sequence, one of the fundamental sequences in MRI is presented. Each line of the diagram represents a different hardware component. The first line refers to the RF transmit coil. The next three lines refer to the gradient coils, slice selection z-gradient, phase encoding y-gradient, and frequency encoding x-gradient, respectively (see section 1.2.5). The last line shows the readout signal, i.e. the MR signal

detected by the RF receive coils. On each line, the vertical axis corresponds to the amplitude and the horizontal axis to the time.
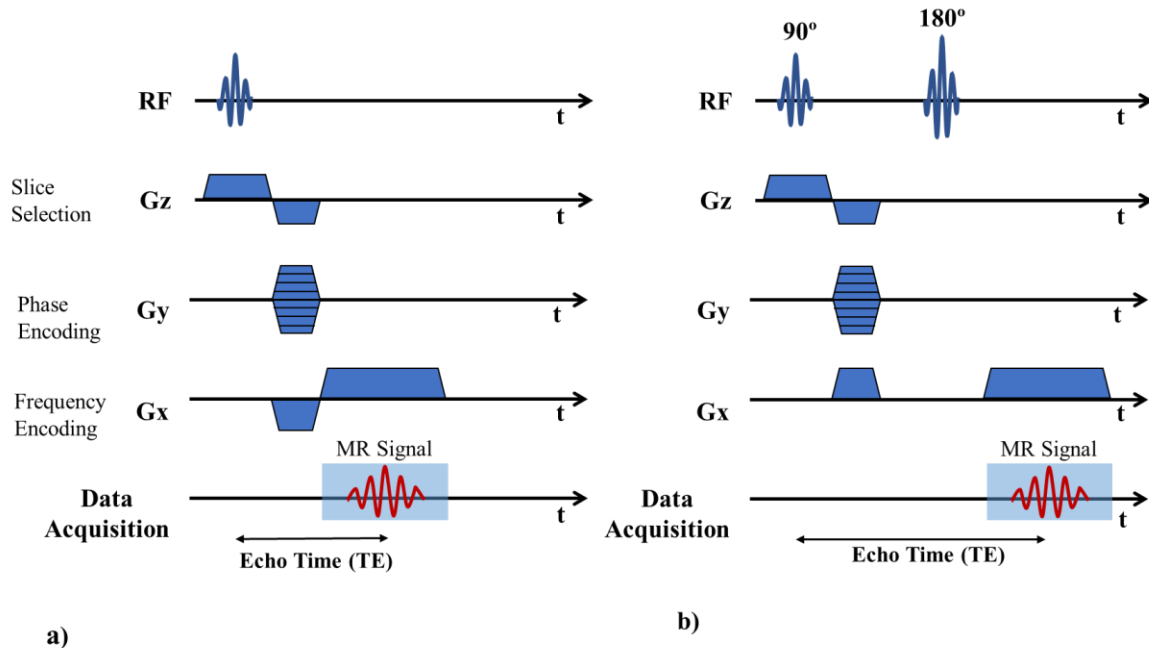
Figure 1.4: *a) Gradient echo sequence scheme. B) Spin Echo sequence scheme, not to scale for illustration purposes*

Every pulse sequence as illustrated in figure 1.4 consists of the following components:

- A slice selection gradient (z-gradient) is applied together with an RF-pulse to excite the target region.
- The y-gradient is switched repeatedly, each time with a different strength, to generate the number of phase shifts across the image. This process is known as phase encoding.
- Echo formation is achieved either by reversing the direction of the magnetic field gradient (Gradient Echo sequences) or by applying a 180º RF pulse (Spin Echo sequences).
- Read-out or data acquisition. The frequency encoding (x-gradient) is switched on and the MR signal is recorded.

Whereas Gradient Echo and Spin Echo sequences are the major sequence families in MRI, more advanced sequences are used in the clinical environment. Moreover, the scientific community continues developing more sophisticated imaging schemes in order to extend the flexibility of MRI to manipulate image contrast, provide spatial localization, suppress signals of particular tissues, excite several slices simultaneously, etc. An extensive description of pulse sequence design can be found in [10].

1.2. Theoretical Background and Principles of MRI

This section gives an overview of the physical basics that make magnetic resonance imaging possible. The main focus is on the most important characteristics of signal generation and image acquisition in MRI. A more comprehensive introduction to the theory of MRI can be found in [10]–[12].

Note that in the nomenclature used in MR the quantity B is usually referred to as the "magnetic field" even though the correct physical term is "magnetic flux density". Both quantities are connected by:

$$\vec{B} = \mu_R \cdot \mu_0 \cdot \vec{H}$$

where μ_R is the dimensionless relative permittivity and μ_0 the permeability of the vacuum. The dimensions of both quantities are:

$$[\vec{B}] = \frac{Vs}{m^2} \qquad\qquad [\vec{H}] = \frac{A}{m}$$

1.2.1. Origin of the MRI Signal: The Nuclear Spin

MRI relies on the quantum mechanical phenomenon of Nuclear Magnetic Resonance (NMR). The NMR phenomenon is based on the intrinsic magnetic moment μ possessed by atomic nuclei with a spin angular momentum or simply "spin", denoted by the letter I.

$$\vec{\mu} = \gamma \hbar \vec{I}$$

where $\hbar$ is the Planck's constant and γ is the gyromagnetic ratio of the considered atomic nuclei. In clinical MRI, most commonly hydrogen nuclei (single protons) are imaged because of their natural abundance in water (H_2O) and lipid molecules (CH_2) in human tissues. The ${}^1H$ nucleus, has I = ½, and the gyromagnetic ratio of protons in water is γ (${}^1H$) = 42.58 MHz/T.

When this magnetic moment is in the presence of an external magnetic field $\vec{B}_0$, it has a magnetic energy E defined by:

$$E = -\vec{\mu} \cdot \vec{B}_0$$

The direction of angular momentum arising from nuclear spin is quantized. For a nucleus with spin I, there are 2I + 1 possible orientations. Hence for the ^{1}H nucleus, there are 2 possible spin states. These states are commonly denoted as $|+\frac{1}{2}\rangle$ and $|-\frac{1}{2}\rangle$ and often referred to as "spin-up" or "parallel" and "spin-down" or "anti-parallel" respectively. The energy difference between the two nuclear spin states, considering the external field $\vec{B}_0$ parallel to $\vec{\mu}$, is:

$$\Delta E = \Delta E_{-1/2} - \Delta E_{+1/2} = \hbar \gamma B_0$$

This effect is known as the nuclear Zeeman splitting [13]. On the other hand, the Planck-Einstein relation reflects that energy states are also discretized and transitions between these energy states can occur via emission or absorption of a photon with the frequency, ω_0:

$$\Delta E = \hbar \omega_0$$

The combination of these two equations reveals the important relationship between the resonance frequency and the applied field strength, the so-called Larmor equation:

$$\omega_0 = \gamma B_0$$

The fact that Planck's constant disappears from the solution implies that a non-quantum interpretation using classical physics is also possible. Based on the classical physics, it can be understood as in presence of a magnetic field $\vec{B}_0$, the magnetic moment of each nucleus experiences a torque and tends to align with the field, precessing at the "resonant" or Larmor frequency ω_0.

Besides the external magnetic field and the gyromagnetic ratio, the Larmor frequency also depends on the immediate chemical environment. Variations in the electron distribution of chemical species can cause slightly different magnetic shielding which leads to a shift of the locally observed magnetic field $\vec{B}_0$. The relative difference in the resonance frequency of one species to a reference resonance frequency is called chemical shift [14]. As an example, the chemical shift between hydrogen nuclei in water and in fat (lipids) is about 3.35 ppm.

1.2.2. The Magnetization Vector and Signal Intensity

From a macroscopic view, the source of the MR signal is the magnetization vector $\vec{M}$ which can be calculated as the sum of magnetic moments in a sample. Since the energy difference ΔE between the two energy states is small in relation to the thermal energy $k_B T$, the probability of the nuclear spins occupying either orientation is nearly identical. However, there is a slight excess of nuclear spins with parallel alignment, which corresponds to lower potential energy. This small imbalance produces net magnetization in the direction of the external magnetic field, governed by the Boltzmann distribution, which is given by:

$$\overrightarrow{M_0} = \frac{1}{V}\sum \overrightarrow{\mu_\iota} = \frac{\gamma^2 \hbar^2}{4 k_B T}\rho_0 \overrightarrow{B_0}$$

where k_B is the Boltzmann constant, T is the absolute temperature in Kelvin and ρ_0 is the physical spin density (number of spins per volume).

At T = 300 K and B_0 = 1.5 T, the spin excess is only about 5 out of a million. Nonetheless, the large number of nuclei in the sample volume creates a measurable macroscopic magnetization, which is directly proportional to the observed MR signal intensity S. Consequently, MR images exhibit a signal intensity directly proportional to the physical spin density:

$$S \propto M_0 \propto \rho_0$$

The magnetization vector is not totally aligned to the main magnetic field $\vec{B}_0$, but precesses around its axis with the Larmor frequency ω_0. The transverse component $\overrightarrow{\mathbf{M}}_{\mathbf{xy}}$ of $\overrightarrow{\mathbf{M}_0}$ can be defined as: $\overrightarrow{M}_{xy} = \overrightarrow{M_0} \sin \alpha$

It is useful to define the longitudinal direction as the direction along the axis of the main magnetic field $\vec{B}_0$, and transverse plane as the plane that is the perpendicular plane to $\vec{B}_0$. Conventionally, the z-axis corresponds to the longitudinal direction while the x-y plane is the transverse plane (Figure 1.5).
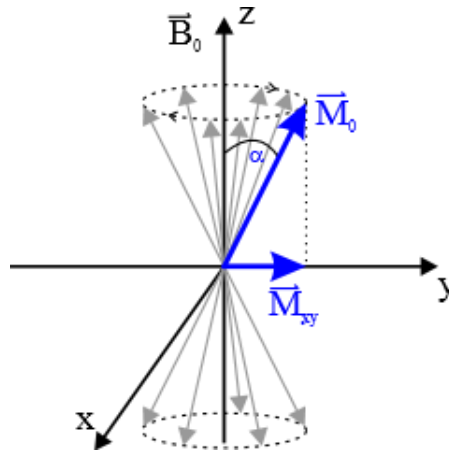
Figure 1.5: *Illustration of the magnetization vector* $\overrightarrow{\mathbf{M}_0}$ *in a magnetic field B₀ along the z-axis and* $\overrightarrow{\mathbf{M}}_{xy}$ *its transverse component related to angle α.*

1.2.3.   The Radiofrequency Field: Excitation of Nuclear Spins

MRI requires the magnetization vector to be tipped away from equilibrium to generate a signal. This phenomenon is achieved by applying a rotating magnetic field perpendicular to the static magnetic field. This excitation field has to match the Larmor frequency as demanded by the resonant condition. For conventional MRI, the Larmor frequency lies in the radiofrequency (RF) range.

The magnetic component of the RF wave is referred to as the transmit RF field: $\vec{B}_1$. In general, the $\vec{B}_1$ field can be decomposed in a longitudinal field $B_{1z}(\vec{x})\vec{e}_z$ with unity vector $\vec{e}_z$ pointing in the longitudinal direction, and two counter rotating components $B_1^-(\vec{x})\vec{e}_-$ and $B_1^+(\vec{x})\vec{e}_+$ of the transversal field $B_{1xy}(\vec{x})\vec{e}_{xy}$. Excitation of spins is performed by the circularly polarized component and $B_1^+(\vec{x})\vec{e}_+$ only, which rotates in the same direction as spins precess. This component is called the active field and is often simply called B_1 field. Although B_1^+ is not equal to the RF field, it is often used synonymously because it is the only component involved in spin excitation.

The definition of a reference frame that rotates with the Larmor frequency helps to understand this process. In the laboratory frame, an external field B_1 rotating with the Larmor frequency corresponds to a static field in the rotating frame. Here, the trajectory of the magnetization vector M can be interpreted as precession around B_1 with the Larmor frequency. In the rotating frame, the static magnetic field $\vec{B}_0$ can be neglected, as it is already accounted for by the frame selection.
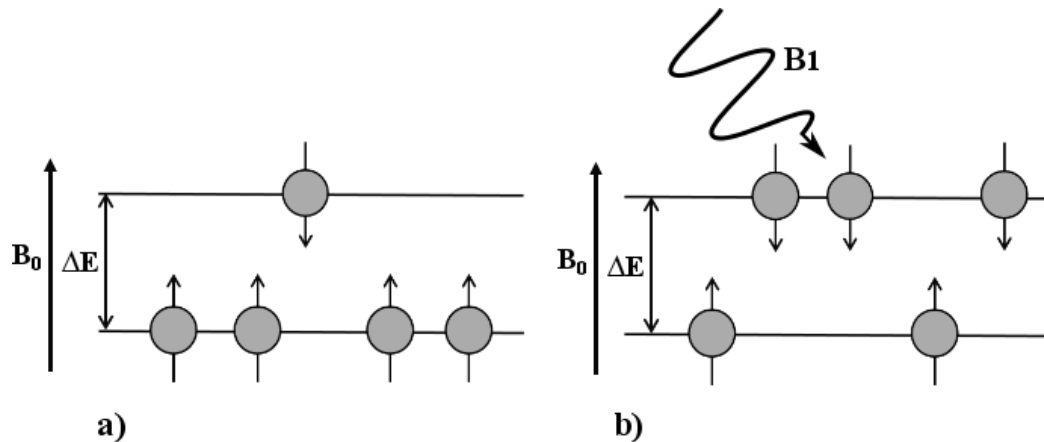

Figure 1.6: *a) A spin in the presence of a magnetic field may align itself either into a parallel or an anti-parallel state. The energy difference of the states is the origin of nuclear magnetic resonance. b) Spins can be excited into the higher, anti-parallel energy state by applying an external field B_1, rotating with the Larmor frequency.*

A B_1 field applied on-resonance for a short period of time is called an RF pulse. Between the modulus of the active field $B_1^+(\vec{x})$ and the flip angle $\alpha(\vec{x})$ of an amplitude modulated RF pulse the following well known relationship is given:

$$\alpha(\vec{x}) = \gamma |B_1^+(\vec{x})| \int_0^T f(t)\, dt$$

with γ being the gyromagnetic constant, T being the pulse duration and f(t) the shape of the applied RF excitation pulse. In MRI pulse sequences, typically, flip angles up to 90 degrees are used. In the spin echo pulse sequence, an $\alpha = 180$ flip angle is applied for spin rephasing.

1.2.4. Relaxation

After the application of the RF pulse, the magnetization vector changes its alignment with respect to the main magnetic field. By switching the RF pulse off, the spins begin to emit the absorbed energy and the magnetization reverts to the thermal equilibrium state. This time-dependent evolution of the macroscopic magnetization is called relaxation and is described by the Bloch Equations [1]:

$$\frac{d\vec{M}}{dt} = \gamma \vec{M}(t) \times \vec{B}(t) - \vec{R}[\vec{M}(t) - \vec{M}_0]$$

where $\vec{B}$ is the total magnetic field, i.e. the superposition of B_0 and B_1 and $\vec{R}$ is the relaxation matrix:

$$\vec{R} = \begin{bmatrix} 1/T_2 & 0 & 0 \\ 0 & 1/T_2 & 0 \\ 0 & 0 & 1/T_1 \end{bmatrix}$$

The components of $\vec{R}$ are called relaxation rates. T_1-relaxation is the energy loss of spins to the surrounding environment or lattice, also called spin-lattice relaxation. It describes the

relaxation of the longitudinal component $\vec{M}_z$ of the magnetization $\vec{M}$ to the magnetization at thermal equilibrium M_0 by:

$$\vec{M}_z(t) = M_0 \cdot (1 - e^{-\frac{t}{T_1}})$$

For the transversal relaxation with the decay process of M_{xy} the solutions yield:

$$\vec{M}_{xy}(t) = M_0 \cdot e^{-\frac{t}{T_2}}$$

The transversal T_2-relaxation refers to the loss of magnetization due to dephasing. This loss of coherence phase is driven by spin-spin interactions, therefore also referred to as spin-spin relaxation.

For a better understanding of the meaning of T_1 and T_2, T_1 can be described as the time needed after a 90° pulse for the longitudinal magnetization to recover 63% of its initial equilibrium magnetization. On the other hand, T_2 describes the point of the decay, when only 37% of the initial transverse magnetization remains.

$$M_z(T_1) = 0.63 M_0$$
$$M_{xy}(T_2) = 0.37 M_0$$

Both values are included in figure 1.7, which depicts the evolution of the longitudinal and the transversal magnetization over time, after an RF pulse is applied.

Mathematically, it takes an infinite amount of time for the longitudinal magnetization to fully recover to M_0 and to the transverse magnetization to completely disappear. In practical terms, however, the longitudinal magnetization is 95% recovered after a time interval equal to $3T_1$, 99% recovered after $5T_1$, and 99.9% recovered after $7T_1$. Similarly, after $3T_2$ the transverse magnetization is at 5% and after $4T_2$ is at 1% of its original strength.
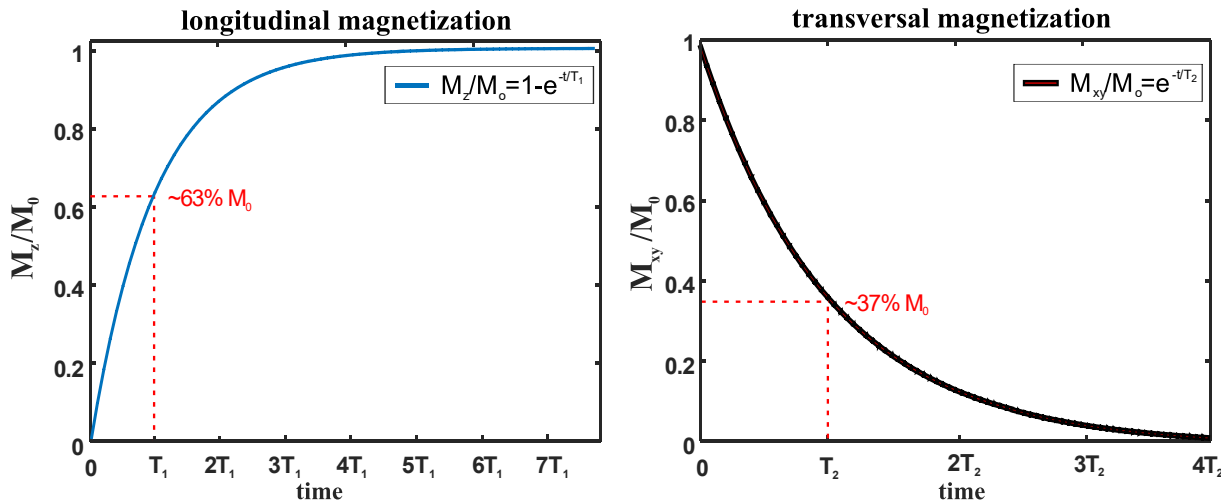
Figure 1.7: *Relaxation curves after a 90º pulse. a) Evolution of the longitudinal magnetization. b) Evolution of the transversal magnetization.*

Table 1 gives some example T_1 and T_2 values of human tissue at 1.5T and 3.0T. Differences between tissues are a consequence of microstructural differences in tissue composition. These differences provide a primary mechanism for differentiating between tissues and lesions when performing MRI. While T2 values are only slightly affected by increasing the magnetic field strength, T_1 relaxation times are prolonged as the field strength increases.

	1.5T		3.0T	
	T_1	T_2	T_1	T_2
Blood	1388	309	1985	275
Heart Muscle	1026	42	1355	47

Table 1: *T_1 and T_2 relaxation times in milliseconds at B_0=1.5T and B_0=3.0T for relevant human tissues in cardiac imaging. Literature data from [15].*

Nevertheless, there is another cause of transverse magnetization dephasing beyond true T_2 effects; namely: field inhomogeneities of the external static magnetic field across the sample

(ΔB_0). In real experiments, the parameter T_2* includes all these contributions that decrease transverse magnetization:

$$\frac{1}{T_2^*} = \frac{1}{T_2} + \gamma\pi\Delta B_0$$

In extremely homogeneous magnetic fields, T_2* values are approximately equal to T_2 values. Otherwise previous equations to describe the relaxation processes are valid by replacing T_2^* by T_2.

After becoming acquainted with the origin of the MR signal and the relaxation processes, the next section will continue explaining how to manipulate those signals to obtain MR images.

1.2.5. From Signal to Image: MR Encoding and k-space Sampling

The assignment of a spin at a spatial location to a unique Larmor frequency is called spatial encoding. This is achieved by superimposing a constant magnetic field gradient, $\vec{G}$ to the existing main magnetic field in all three dimensions:

$$\vec{G} = \left(G_x, G_y, G_z\right) = \left(\frac{\partial B_z}{\partial x} + \frac{\partial B_z}{\partial y} + \frac{\partial B_z}{\partial z}\right)$$

The Larmor frequency becomes a function of the location $\vec{r}$ with:

$$\omega_0(\vec{r}) = \gamma\left(B_0 + \vec{G}\vec{r}\right) = \gamma\left(B_0 + \frac{\partial B_z}{\partial x}\vec{x} + \frac{\partial B_z}{\partial y}\vec{y} + \frac{\partial B_z}{\partial z}\vec{z}\right)$$

The time dependent NMR-signal amplitude S(t) depends now on the spin density of the volume $\rho(\vec{r})$ and its spatial Larmor frequency at position $\vec{r}$:

$$S(t) = \iiint \rho(\vec{r})\, e^{i\gamma\vec{G}\vec{r}t}\, d\vec{r}$$

By introducing the spatial frequency, $\vec{k}$:

$$\vec{k} = \frac{\gamma \vec{G} t}{2\pi}$$

the MR signal (S) becomes:

$$S(\vec{k}) = \iiint \rho(\vec{r}) \, e^{i2\pi \vec{k}\vec{r}} \, d\vec{r}$$

This means that the measured signal is simply the Fourier transform of the spin density $\rho(\vec{r})$ at the frequency coordinate k(t) determined by the magnetic field gradients. Accordingly, the spin density can be calculated taking the reverse transform:

$$\rho(\vec{r}) = \iiint S(\vec{k}) \, e^{i2\pi \vec{k}\vec{r}} \, d\vec{k}$$

In MRI, the application of magnetic field gradients differentiates between "slice selection," "phase encoding," and "frequency encoding" as described in section 1.1.2.

Slice selection. When the G_z gradient is applied during the RF pulse only spins in a thin subvolume are excited rather than in the entire subject. The slice thickness is defined by the bandwidth of the RF pulse and the amplitude of the slice-selection gradient.

Phase encoding. If a constant gradient G_y is applied to the sample, the frequency of precession will change linearly with the location, too. When a gradient field is applied in the y-direction for a given time interval, the Larmor frequency will vary in this direction during that time interval, so that the signal at different positions accumulates a different phase. After the gradient has been switched off, the precession frequency returns to a constant value over the plane, while the imprinted phase remains proportional to y. This process is called phase encoding.

Frequency encoding. If the signal is read out while G_x is on, contributions from different locations along the x-axis will exhibit different frequencies. This process is called frequency

encoding, and the corresponding gradient is called frequency encoding gradient, also sometimes referred to as read gradient.

By convention, the space covered by the frequency and phase data is referred to as the raw data matrix or "k-space." The units of k correspond to [cycles/cm]. This brings us to the fundamental underlying principle of MRI: An MR image is composed of spatial frequencies, which is a measure of how rapidly the image intensity varies over space. MRI raw data are samples of the Fourier Transform (FT) of the imaged object, and by performing an inverse FT operation on the raw data, the desired image can be recovered. This relationship is depicted in figure 1.8 the image reconstruction is simply done by applying the inverse-Fourier transform to the detected signal.

Every point in the k-space contains part of the information for the complete image. A point in k-space does not correspond to a point in the image domain. The inner rows of the k-space, the low spatial frequencies, provide information on the overall intensity and general features of an image while the outer rows of the k-space, the high spatial frequencies, provide information regarding the borders and edges of the image, the detail of the structures.

In a Cartesian acquisition scheme, the phase- and frequency encoding gradients are applied prior to and during signal sampling respectively; k_x and k_y are the coordinates in the k-space domain.

For each encoding step n_y, the free induction decay (FID) provides one line in the k-space of N_x sample points (figure 1.9). After N_y iterations with a repetition time TR, a full 2D grid is sampled and an image of spin density $\rho(x, y)$ can be reconstructed by 2D inverse Fourier transformation.
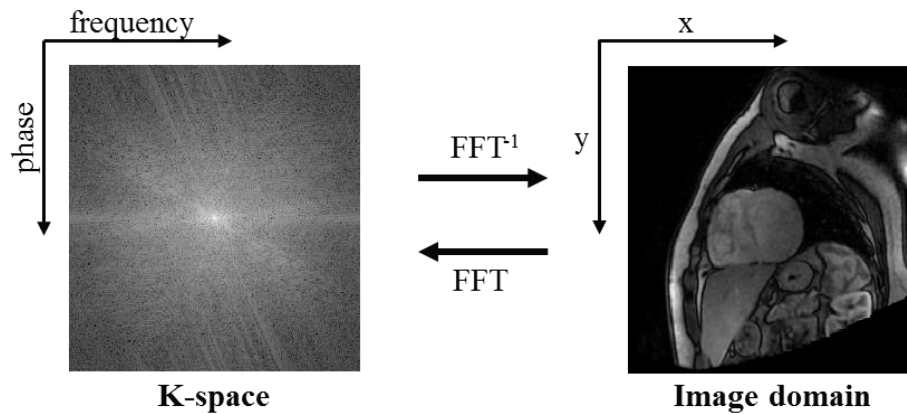
Figure 1.8: *a) Raw data in k-space array and b) corresponding image data*

Different pulse sequences may acquire the k-space data in a different order, and the path taken to sample k-space data is known as the k-space "trajectory." The most frequently used pulse sequences sample k-space one line at a time on a Cartesian grid. However, the acquisition of data in k-space is not limited to the rectilinear Cartesian sampling. In fact, there is considerable freedom how to acquire data in MRI. By altering the encoding gradients in an appropriate way, one can achieve more sophisticated trajectories such as radial or spiral.
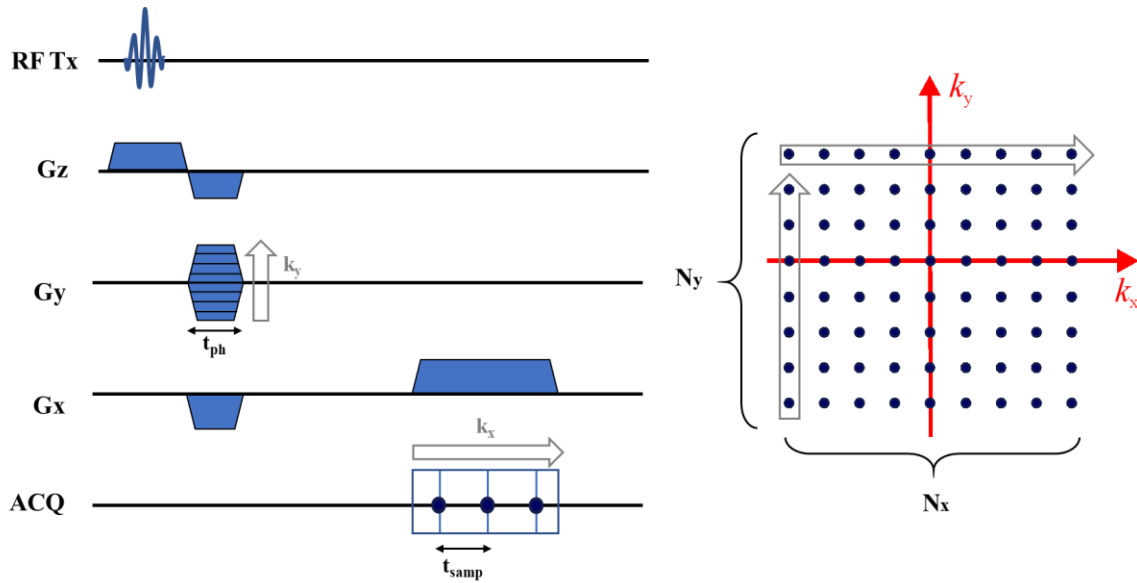
Figure 1.9: *Schematic of a MRI pulse sequence with k-space sampling; RF Tx = RF excitation, G_z=slice selective gradient, G_y=phase encoding gradient, G_x= frequency encoding gradient, ACQ=acquisition window, N_x, N_y=k-space matrix size, t_{ph}=phase encoding duration, t_{samp}= sampling time.*

1.3. Cardiac MRI

1.3.1.   Review of Basic Anatomy and Physiology of the Heart

This section describes the basic aspects of anatomy and physiology of the human heart as well as the standardized nomenclature required for a comprehensive understanding of this thesis and the interpretation of cardiac MR examinations.

Anatomy and heart function

The central muscle of the cardiovascular system is divided into two halves, the left side where the venous blood circulates and the right side where the arterial blood circulates. Each of them contains two chambers: the ventricles and the atria. The lower right ventricle forwards deoxygenated blood via the pulmonary circulation system where it is enriched with oxygen. The oxygenated blood is then pumped by the left ventricle into the aorta and the arterial circulation system. A wall known as the septum separates the left side of the heart from the right side and each chamber is closed off by a one-way valve which controls the blood flow between the atria, the ventricles and the arteries.

The heart is comprised of three different layers of muscular tissue. The myocardium is the middle layer, located between the outer epicardial layer and the inner endocardial layer. These layers are responsible for the processes of contraction and relaxation of the cardiac walls.
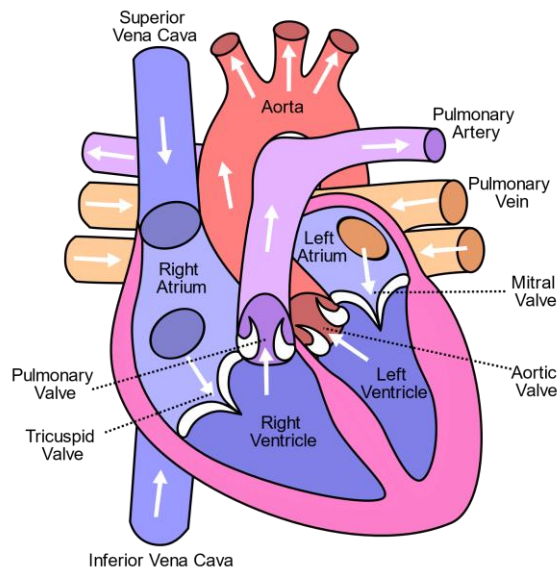

Figure 1.10: *Anatomy of the human heart.*

Cardiac physiology and electric activity

The mechanical contraction of the heart is induced by electrical activation of the muscle itself. This change of electric potential can be measured by an electrocardiography (ECG) recording on the chest surface. The adult heart performs between 40 and 80 contractions per minute i.e. beats per minute (bpm) at rest and up to 180 to 200 bpm under stress. This corresponds to a motion frequency of 0.83Hz to 3.33Hz. The heart cycle can be split into two phases - the systole and the diastole respectively.

Considering the ventricular systolic phase as the initial state of the cardiac cycle, this phase starts with the left ventricle at is maximum volume and the aortic and mitral valves closed. Isovolumetric contraction increases the pressure in the left ventricle until it reaches the aortic

pressure. Then, the aortic valve opens and the left ventricle ejects the blood into the circulatory system. At this point, the myocardium is thicker. The ECG represents this activation in the PR interval (atria activation) and the QRS complex (ventricle contraction) as shown in figure 1.11. The systolic phase lasts approximately between 270ms and 160ms at 65bpm and 200bpm respectively [16]. In the diastole, the heart muscle relaxes and blood flows from the atria into the vessels. About 70% of the blood volume flows passively into the ventricles, while the rest is pushed in the early systolic phase by atrial contraction. This phase lasts approximately 530ms and 140ms respectively, and is represented in the ECG by the ST and TP segments. During the end-diastolic phase, the heart motion is at its minimum. For high-resolution CMR, this period is the preferred state for image acquisition.
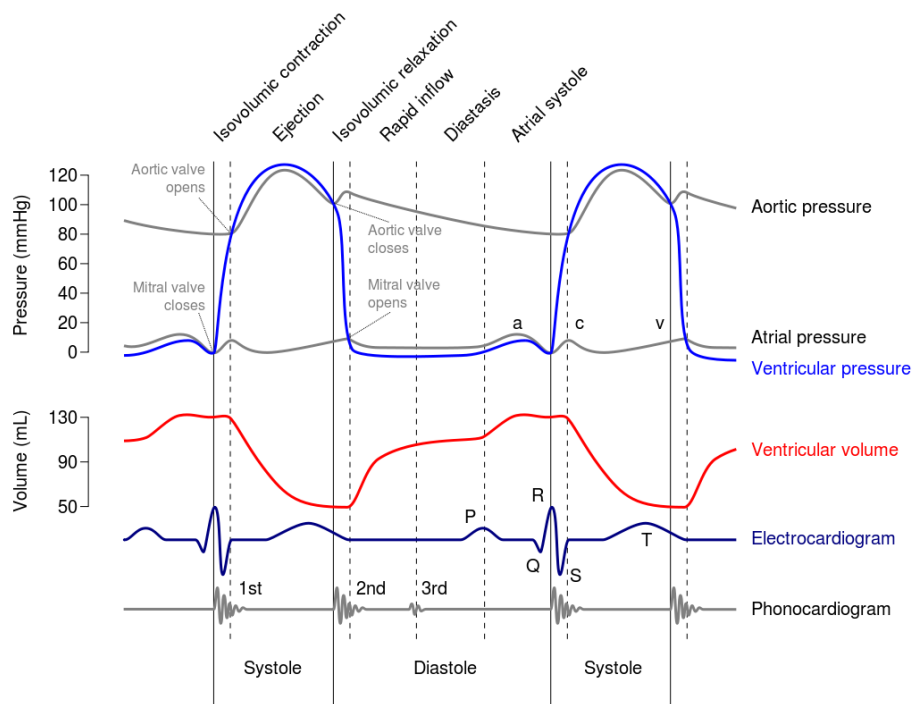

Figure 1.11: *Wiggers diagram of cardiophysiologic pressure and flow.*

1.3.2.   Importance of the Imaging of the Heart

Heart failure and cardiovascular diseases are one of the most common causes of hospitalization in developed countries with an estimated prevalence of 2-3% in the general population and 10-20% in those aged over 70 years [17]. While this section has no pretense at reviewing all cardiac pathologies, it seems important to cite some of them within a general classification for a better understanding of the value of CMR as a diagnostic tool.

- Diseases involving coronary circulation, also known as ischemic heart diseases. This group of diseases includes myocardial infarction or atherosclerosis which is a gradual clogging of the arteries over many years by calcification, fatty materials and other substances in the blood stream.

- Diseases involving mechanical problems of the heart muscle. For example, cardiomyopathies. An enlargement of the heart due to thickening or weakening of the heart muscle. Aneurysms, a dilation of a part of the heart muscle or the aorta which may cause weakness of the tissue also belong to this group.

- Diseases of the cardiac electrical activity, e.g. arrhythmias.

- Defects in anatomical structures i.e. congenital heart diseases: anomalous coronaries, valves…

Cardiovascular magnetic resonance (CMR) provides relevant morphologic and functional information for the diagnosis of different heart diseases. Morphological diagnosis includes imaging of the heart valves, wall thickness or size of the heart. Functional imaging refers to the analysis of heart motion throughout the cardiac cycle or blood flow in the coronary arteries. The most frequent clinical indications for CMR are risk stratification in ischemic heart diseases [18], medical examination of cardiomyopathies and assessment of viability [19]. Also in rare diseases like amyloidosis and congenital heart diseases, CMR has demonstrated its usefulness [20]. Especially, the characterization of the myocardial tissue including the detection of edema and fibrosis is a unique feature of CMR [21].

Examination protocols include imaging techniques such as contrast enhancement imaging [22], which allows to quantify myocardial infarct size; cardiac perfusion which evaluates the extent of microvasculature injury; quantitative imaging (T_1, T_2 mapping) which provides more fine information on myocardial architecture [23]. Regarding interventional procedures, MRI also allows the detection of scar tissue, which is important for catheter-based ablations [24]. Thus, cardiac MRI is nowadays one of the most important imaging modalities for cardiac assessments. Its increasing use in clinical routine helps clinicians to establish accurate diagnosis, risk stratification, therapeutic decision making and monitoring therapeutic efficacy.

1.3.3.   Challenges in Cardiac Imaging

Cardiac planes & AHA representation

The standard imaging planes are axial, coronal and sagittal. All examinations include a localizing scan which uses these predefined orientations. However, the complex orientation of the heart within the thorax, requires imaging in specific planes i.e. short axis, vertical long axis, and horizontal long axis are used for an accurate assessment of the cardiac structures. These planes are perpendicular to each other as can be seen in figure 1.12.
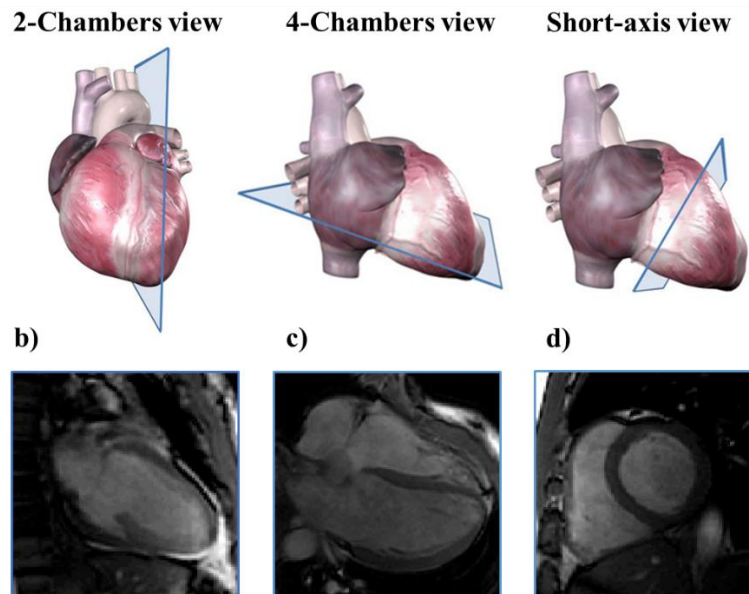

Figure 1.12: *Schematic view of the three most basic cardiac planes and their corresponding MR images: a) 2-chambers of vertical long axis view, b) 4-chambers or horizontal long axis view and c) short axis view.*

This is actually the first challenge of cardiac imaging for any modality. In a typical clinical setting the first 10-15 minutes are only dedicated to localize the right cardiac plane for a specific subject without obtaining any diagnostic information.

This thesis is primarily directed at the study of the left ventricle and the characterization of the myocardium due to their importance in the cardiac function. A short axis view showing a cross section of the ventricles and the left ventricular myocardium will be the reference view for the purpose of this study.

Because of the variety of imaging modalities and associated spatial resolutions, research and clinical applications require consensus by means of a standardized segmented heart model. For this purpose, the American Heart Organization (AHA) recommends using 17 segments at different short axis locations and circumferential positions of the left ventricle, as illustrated in figure 1.13.
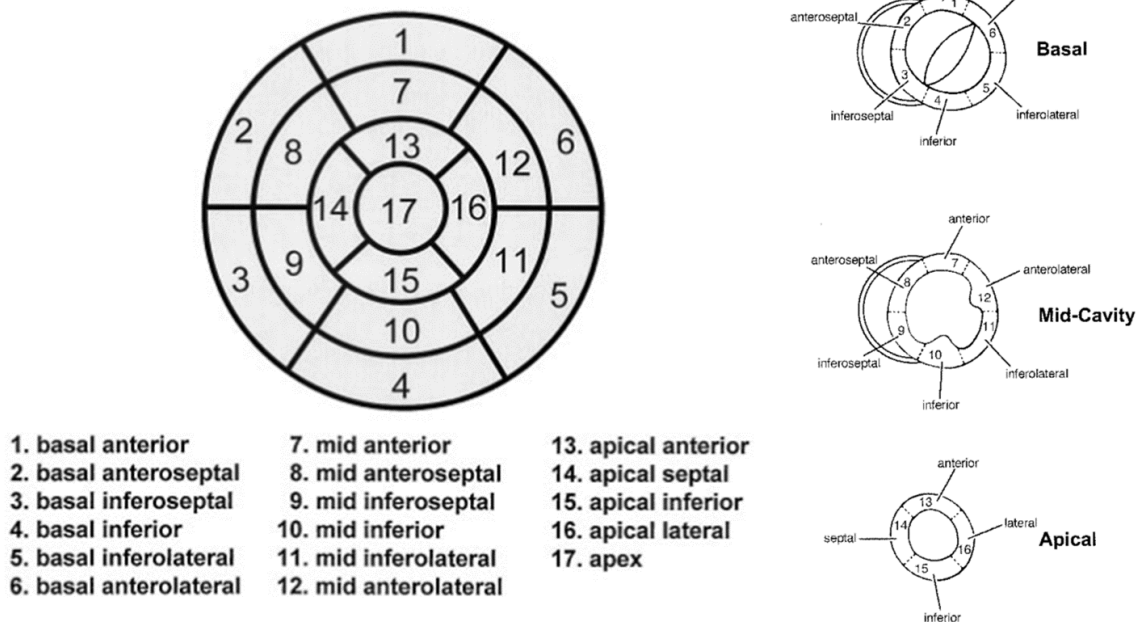

Left Ventricular Segmentation

1. basal anterior
2. basal anteroseptal
3. basal inferoseptal
4. basal inferior
5. basal inferolateral
6. basal anterolateral
7. mid anterior
8. mid anteroseptal
9. mid inferoseptal
10. mid inferior
11. mid inferolateral
12. mid anterolateral
13. apical anterior
14. apical septal
15. apical inferior
16. apical lateral
17. apex

Figure 1.13: *Standardized myocardial segmentation for the left ventricle using 17 regions as suggested by the AHA [25]. The basal and mid-ventricular short axis views are divided in six circumferential sectors, the apical slice consists of four sectors. The apex can be regarded as a single 17th segment. The reference for angular orientations is the right ventricle.*

Physiological Motion in cardiac MRI

Motion of the heart is the vector sum of three components: motion caused by the pumping of the four chambers, motion caused by respiration and any additional voluntary or involuntary bulk patient movement.

The two former components are periodic and relatively predictable while the latter is usually a one-time event that occurs randomly and in an unpredictable pattern. In general, motion leads to blurring in the images and results in discontinuities of data in the k-space domain, which leads to additional image artifacts [26]. This is not only detrimental to image quality, but also affects the diagnostic quality of MRI.

Ideally, the content of an imaged volume should be rigid and motionless at the time of image data acquisition. Simultaneously, if the image data collection is divided into multiple k-space segments acquired at different time points, it is necessary that the object remains stationary at the time of data collection. However, these conditions are not easily met due to the relatively prolonged time required for MRI.

In the following, the principal sources of motion in CMR are described, followed by an overview of commonly used motion compensation strategies.

Compensating for cardiac motion:

Generally, artifacts due to the rhythmic pumping of the heart are addressed by the so-called cardiac gating. During the cardiac cycle, there are two periods of minimal heart motion. A period of minimal motion occurs during mid-diastole although end-systolic imaging may be preferable for patients with high heart-rates [27]. Cardiac MRI is commonly performed during one of these rest periods to minimize the adverse effects of motion during data acquisition. The time of least cardiac motion and thus the trigger delay can be estimated from the patient's heart rate [28] or visually determined from a cine sequence [29]. The duration of the rest period is usually not sufficient to collect all necessary data in k-space [30]. Therefore, data are acquired

over a number of cardiac cycles, synchronizing the patient physiological signal (R-wave) and the MR data collection. The R-wave can be monitored using different sensor mechanisms. Typically, these are electrocardiogram (ECG) or photoplethysmography (PPG).

ECG – Electrocardiography

The electrocardiogram (ECG) reflects changes in electrical potential of the conduction system of the heart which induces its mechanical contraction. It is measured by using MR-compatible electrodes attached to the patient's chest using sticky pads with conductive jelly.

PPG - Photoplethysmography

PPG measures changes in blood volume in a portion of the peripheral microvasculature, commonly a fingertip. This technique uses electrical signals derived from light reflected due to changes in blood flow during heart activity. As the heart contracts, blood pressure within the left ventricle increases. This increase forces a pressurized "pulse" of blood into the arteries of the body, which causes them to swell slightly before once again returning to their previous state. By shining a light on a patch of skin with an LED light source, the increased pulse pressure will cause a measurable difference in the amount of light reflected back a light sensor.
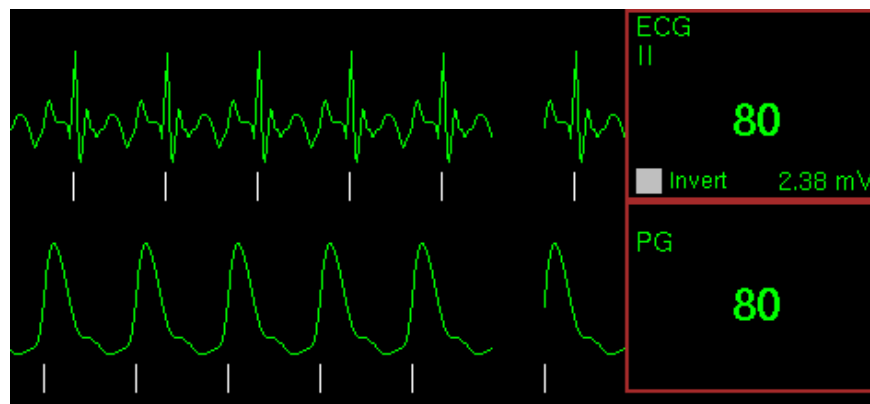
Figure 1.14: *ECG and PPG monitoring at the scanner user interface. White marks represent the R-wave peaks which trigger data acquisition.*

ECG triggering is usually preferred because it is a direct measurement of the electrical signal of the cardiac cycle (QRS complex), the delays from the R-wave to the trigger are less variable and it is more robust and accurate. However, considerable ECG-signal degradation may occur due to the so-called magnetohydrodynamic effect, which creates an artificial voltage overlaid on the T-wave and may mislead the right trigger detection. The magnetohydrodynamic effect occurs in the presence of a static magnetic field because blood is an electric conductor fluid and its motion produces an electric current which adds on to the cardiac conduction signal. This effect increases with magnetic field strength and presents a major challenge at 7T and beyond [31].

As an alternative to ECG and PPG other triggering strategies have been described, such as acoustic triggering [32] or laser Doppler velocimetry [33]. Moreover, self-gating techniques have also emerged. Here, motion information is directly extracted from parts of the acquired image data itself [34].

Cardiac gating can be performed in two different ways:

- Prospective gating uses the R-wave to initiate (trigger) the acquisition of the image data and allows imaging during a specific user-selected acquisition window.
- Retrospectively gating records k-space and the cardiac signal continuously and then assembles k-space into the relevant cardiac phases after the acquisition.

Prospective triggering is more sensitive to variable R-R intervals (arrhythmic patients) and its implementation into the pulse sequence is more complex than retrospective gating. However, for imaging at a single time point in the cardiac cycle it is the commonly used technique since it is more time efficient.

Compensating for respiratory motion:

Unlike cardiac motion, respiratory motion can be suppressed for a limited amount of time. Simple breath holding is still the most common solution in clinical CMR examinations to effectively "freeze" respiratory motion. Several acquisitions are performed during a single or multiple breath-holds, either performed during full inhalation, which is typically more comfortable for the patient, or during expiration, which usually results in lower respiration variability between different breath-holds. The disadvantages of this method are the limited duration of the acquisition, constrained to an average of 10-15s per breath-hold and the requirement of patient cooperation, which can be problematic in different situations as poor tolerance to breath-holding, pediatric patients, anesthesia…

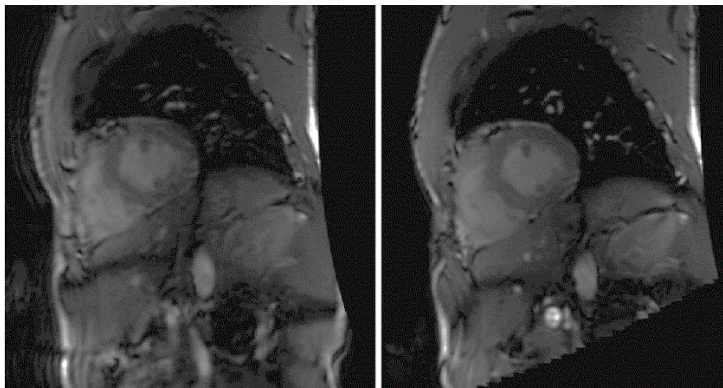
Figure 1.15: *Short axis view acquired in free breathing with blurring due to respiratory motion (left) vs a breath-hold acquisition during expiration (right).*

Another respiratory motion compensation strategy is monitoring respiration. This approach uses an external physiologic device such as a pneumatic belt or optical tracking markers to detect breathing motion. Respiratory gating, prospectively alters data acquisition [35] or retrospectively corrects acquired data based on detected motion [36]. However, such external measurements increase the patient setup time and, furthermore, may not accurately reflect the motion in the volume of interest.

A further development in free-breathing protocols are navigator echo techniques [37], [38]. A detailed overview of navigator approaches can be found in chapter 12.2 of [10]. They have the advantage of using an additional MR scan rather than external sensors to extract motion, usually by monitoring the respiration level based on position of the diaphragm. However, they are not available on every pulse sequence as they require some time in the pulse sequence and need to be explicitly programmed. As a result, navigator sequences are relatively inefficient since they require longer scan times compared to non-navigated sequences.

An alternative to the navigation methodology is self-navigated approaches, which directly extract motion parameters from the imaging data rather than external devices or navigators [39]–[41]. Although the scanning efficiency is improved compared to navigators, self-gating techniques are often limited to specific imaging schemes and have not been used extensively.

<u>Field Inhomogeneities and their effects in cardiac MRI.</u>

There is an ongoing trend in cardiac MRI towards higher magnetic field strengths (B_0) due to higher SNR, stronger tissue contrast and better acceleration performances in parallel imaging tissues [42]–[44]. Nowadays, most clinical MR scanners operate at a B_0 field of 1.5 T or 3.0T. 1.5T is considered a standard field and 3.0T is considered "high field". During the last years a strong interest in 7T, considered "ultra-high field", has resulted in several tens of 7T scanners installed at different research institutes around the world with a growing number of clinical research studies at 7T published every year. Despite of the gains of high field strengths systems, imaging protocols require careful consideration of possible field inhomogeneities.

All electromagnetic waves travel at the speed of light, *c*. This speed is defined as the product of the wavelength (λ) and frequency (*f)*, and is determined by the permittivity (ε) and permeability (μ) of the propagating medium, as in the following equation:

$$\frac{c}{\sqrt{\mu\varepsilon}} = \lambda \cdot f$$

As the frequency is fixed at the Larmor frequency, the wavelength of the radiation varies as a function of the underlying electromagnetic properties. In vacuum, the wavelength of Larmor frequency radiation at 3.0T is approximately 2.3m. However, in human tissue it reduces to approximately 0.26-0.33m, assuming relative permittivities of $\varepsilon_r = 50\text{-}80$ and permeabilities $\mu_r=1$ at RF frequencies [45].

When the wavelength of the RF excitation is comparable to the dimension of the body i.e. the heart at 3.0T, the field will have several spatial cycles across the anatomy. Therefore, fields generated by different parts of the RF coil will combine either constructively or destructively. These interferences vary in space, leading to B_1^+ field inhomogeneity. B_1^+ distortions can obscure physiological variation in signal intensity when the latter are due to alterations of tissue relaxation rates in areas of pathology. This dielectric effect is negligible at field strengths lower than 1.5T and increases in severity at higher B_0 field strengths, as the Larmor frequency is greater, the RF wavelength shorter.

The second interaction effect arises from the electromagnetic response of human tissue. When a human body is placed in the homogeneous B_0 field of an MR scanner, spatial perturbations of B_0 (ΔB_0) will occur, which are mainly induced by the different magnetic susceptibilities of biological tissues and interfaces air-tissue, for example around the lungs. Because these variations are proportional to the B_0, larger susceptibility-induced artifacts occur as the main static field increases [46]. The ΔB_0 also can affect the spatial excitation profile of the RF pulses. The electromagnetic field produced by an RF coil contains both magnetic and electric components. Although human tissue has a very small magnetic response to the RF magnetic field (hence $\mu_r=1$), most tissue are conductive (have a high relative permeability) and the electric field couples strongly to them. The consequences of these mechanisms can be understood in the context of Faraday's Law. Any current driven by the B_1^+ field will induce an additional magnetic field that is partially out of phase with the original. This will alter the total B_1^+ field by changing its amplitude and direction. Again, this mechanism will vary spatially, creating an inhomogeneous B_1^+ field.
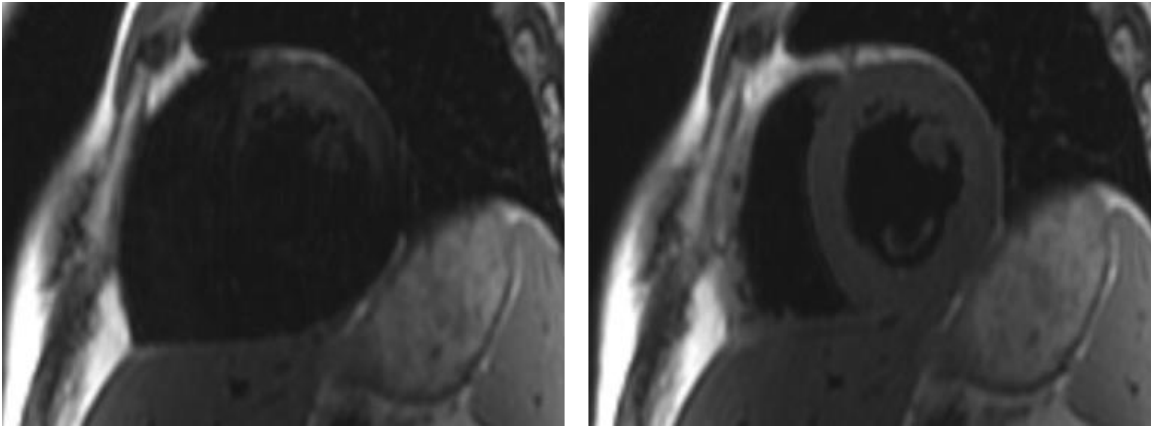
Figure 1.16: *Short axis view presenting shading artifact due to B_1^+ inhomogeneities (left) vs a short axis view with homogeneous tissue contrast.*

Correction of B_0 inhomogeneities is made by proper design and configuration of the coil. Excluding possible metallic implants, cardiac MR scans assume to have homogenous B_0 field by using the so-called B_0 shimming during the scanning protocol. This process involves using shim coils that apply additional magnetic fields to compensate B_0 field variations in a defined volume.

Hereafter, this thesis is focused on the topic of B_1^+ inhomogeneities. They pose a bigger challenge for cardiac MR. Attempts to prospective remove these imperfections are for example the use of adiabatic pulses [47]. They can produce very homogeneous flip angles even for inhomogeneous B_1^+ distributions. However, these pulses tend to be long, increasing both the echo time and the power deposition. Therefore, their efficacy is mainly limited by safety constrains on RF deposition into tissue as well as unwanted magnetization transfer effects. Another method is the positioning of a dielectric cushion or RF pad anteriorly and sometimes posteriorly on the body to passively change the geometry of the B_1^+ field distribution and hence change the phase of the RF standing waves thereby reducing or eliminating the nonuniformity [48]. The pad contains a low conductivity material with a high dielectric constant with an

appropriate doping agent such that the pad does not appear in the MR images. Other methods manually modify the RF-transmitter amplitude in order to reduce the B_1^+ inhomogeneity-induced signal loss. The automatic calibration of the RF-transmitter amplitude may be affected by B_1^+ inhomogeneity effects and an improved flip-angle distribution can be obtained by manually adjusting the transmitter amplitude. In combination with postprocessing filters that provide a more uniform signal distribution, image quality can be considerably improved [49] as long as the knowledge of the actual RF field profile exist. Consequently, an accurate measurement of the spatial distribution of the transmitted RF field, known as B_1^+ mapping, is important for many MR imaging applications to support appropriate correction. The concept of B_1^+ mapping will be discussed extensively in section 3.1.

In conclusion, the heart is a complex system in terms of mechanical, electrical, and physiological mechanisms which are all cross related. Cardiac MR can be regarded as one of the most challenging MRI applications. Currently, MR scans cannot be faster than physiological motion and require the compromise between scan time and spatial resolution. Techniques for motion correction are essential to suppress these artifacts and improve diagnostic quality of the images. In addition to physiological motion, CMR must face a second challenge associated to high field strengths: magnetic susceptibility induced B_0 inhomogeneities and inhomogeneities of the transmit B_1 field, both produced by electromagnetic interactions with the human body. B_1^+ inhomogeneity can cause problems with sequences where an accurate flip angle is required. To overcome this problem, there are several methods that attempt to remove the effect of B_1^+ inhomogeneity in post processing. These can be improved if the B_1^+ field inhomogeneity has been previously mapped. The following section will present a review of the existing B_1^+ mapping techniques and their evaluation with respect to cardiac applications.

1.4. B_1^+ Mapping – State of the Art

This section explains the concept of B_1^+ mapping, describes the most prominent B_1^+ mapping techniques and evaluates these methods with a special focus on the requirements for cardiac applications.

1.4.1.   Introduction to B_1^+ Mapping

Most of the techniques to address the B_1^+ inhomogeneity issue are based on the knowledge of the spatial distribution of the transmitted RF field (B_1^+) across the sample, which is measured using an appropriate mapping technique. Direct mapping of the transmitted field is appealing as it may be incorporated into an imaging experiment in the form of a calibration scan at the beginning of the session, does not require prior knowledge of the dielectric properties of tissues and coil geometry and at the same time is subject specific.

The general idea behind B_1^+ mapping is to determine a pulse sequence that varies only with respect to the B_1^+ field and is not affected by other variations as for example relaxation effects. As described in section 1, the MR image signal intensity depends on many variables.

Therefore, a general strategy is to derive B_1^+ maps from the ratio of two images and use a mathematical operation to cancel out all other undesired characteristics in the image.

In this thesis it was chosen to consider the magnitude of the field as a multiplicative factor of a nominal flip angle α_{nom}. The flip-angle is a measure of signal intensity variations due to the B_1^+ field. Knowledge of the flip-angle is generally the desired outcome from B_1^+ mapping in order to account for the corresponding intensity variations. This means that for an RF pulse of flip angle α_{nom} and B_1^+=0.5 at a specific spatial position, the actual flip-angle that will be applied at that position is equal to $0.5 \cdot \alpha_{nom}$. However, B_1^+ maps could be also expressed in μT or Gauss units.

1.4.2. Description of the main B_1^+ mapping methods

For B_1^+ mapping a variety of methods exist which can be categorized on whether the magnitude or phase of the image is used to estimate the B_1^+ field. In the following subsections the basics of the four most established B_1^+ mapping methods according to the literature are introduced.

Double Angle Method (DAM)

The most simple and straightforward method is the Double Angle Method [50], [51], originally introduced by E. K. Insko and L. Bolinger [50]. It is inherently an image magnitude-based method. The actual flip angle map is derived from the ratio of the signal magnitudes of two images to map B_1^+: one acquired with a nominal flip-angle α and another acquired at a nominal flip-angle of 2α. Two sequences are proposed in [50] a Gradient Echo (GRE) and a Spin Echo (SE) based version.

For the GRE sequence, the signal magnitude has a sinusoidal dependency on flip angle as: $I = M_0 \sin(\alpha)$, where M_0 denotes the magnitude of the thermal equilibrium magnetization. Thus, the actual flip-angle distribution can be calculated as the ratio of the two acquired images:

$$\alpha = \arccos\left(\frac{I_{2\alpha}}{2I_\alpha}\right)$$

The mathematical relationship between the signal magnitude ratio and B_1^+ can be similarly derived for the SE version. Choosing $\alpha_2 = 2\alpha_1$, the signal magnitude is $I = M_0 \sin^3 \alpha$. Therefore, the actual flip-angle distribution can be calculated as:

$$\alpha = \arccos\left(\frac{I_{2\alpha}}{8I_\alpha}\right)^{1/3}$$

The pulse sequence diagram (PSD) used to generate the images for the two versions of the DAM is shown in figure 1.17.
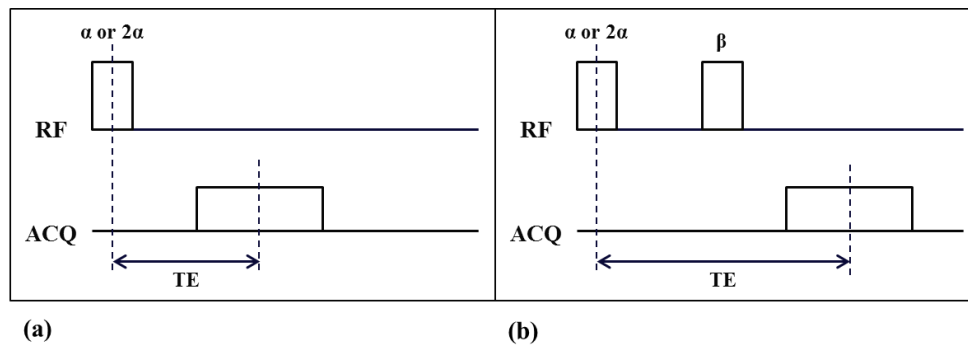
Figure 1.17: *Double Angle Method basic diagram for a) Gradient Echo sequence and b) Spin Echo sequence.*

Although the GRE sequence has a lower sensitivity to small variations in B_1^+, it has a larger dynamic range, making it more suitable for use with the surface coils, where the B_1^+ field is expected to vary more drastically. On the other hand, the SE version presents higher sensitivity to small variations of B_1^+ due to the $\sin^3 \alpha$ dependence. This comes at a trade-off of smaller dynamic range, which in turn makes the method suitable for use when the B_1^+ variation is expected to be small, e.g. in a body coil configuration.

The main disadvantage of the DAM, especially for in vivo applications, is its dependence to T_1. A long repetition time is usually used to achieve complete T_1 recovery. The condition to assume there are no relaxation effects $T_R \geq 5T_1$, results in an extended scan time. For example, for a muscle T_1 of about 1000ms, the repetition time should be 5s. Therefore, a 64x64 resolution map would require a scan time per image of > 5 minutes. Furthermore, T_1 increases with increasing main-field strength, so that both the TR and scan time will be longer for higher field strengths. In addition to this, lengthening the total exam time makes the method sensitive to motion without possibilities of using breath-holding techniques.

In order to overcome the limitation of long relaxation delays between sequence repetitions, a variation of this method was proposed by Cunningham et al [52]. This alternative, named the Saturated Double Angle Method (SDAM), applies saturation pulses at the end of each data acquisition to reset the longitudinal magnetization and a spiral readout reducing the measuring time to the duration of a breath-hold. A drawback of SDAM is a low signal-to-noise ratio (SNR) due to destruction of longitudinal magnetization.

The Actual Flip-Angle Imaging Method (AFI)

The Actual Flip-Angle Imaging Method (AFI) [53] was developed in 2007 by Yarnykh et al. It uses two different TRs rather than different flip-angles. It utilizes a dual-steady state signal and the ratio of those signals. The resulting B_1^+ map can be derived from the ratio of the signal magnitudes of the two acquired images as follows:

$$\alpha = arccos \frac{rn - 1}{n - r}$$

where the ratio of both steady-state signals is $r = {I_2}/{I_1}$ and the ratio of both repetition times is defined as $n = {TR_2}/{TR_1}$.
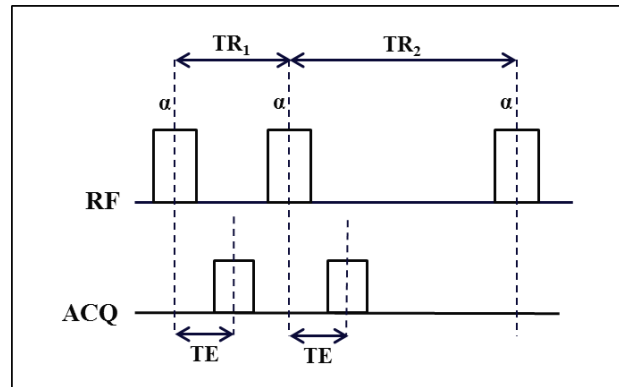
Figure 1.18: *Actual flip-angle imaging method pulse sequence diagram. The sequence consists of a flip-angle α, separated by two interleaved TR periods: TR_1 and TR_2.*

The short TRs used in the AFI method make the method suitable for fast imaging. For example, if $TR_1/TR_2 = 20/40ms$, a 64x64 B_1^+ map can be acquired in about 7.5s. Possible limitations of the AFI method are related to the GRE nature of the acquired signals. These include the sensitivity of the signal to main magnetic field nonuniformities, chemical shift, and flow.

Bloch-Siegert Shift Method (BSS)

The Bloch-Siegert Shift Method [54] exploits the fact that the application of an off-resonance RF pulse slightly changes the effective frequency of spins that are on-resonance. The slight difference in effective frequency causes the previously excited magnetization to gain phase over the duration of the RF pulse. BSS employs a GRE sequence with a strong off-resonance pulse inserted between excitation and acquisition, which introduces the B₁ dependent shift.

Two images are acquired with opposite offset frequencies usually $\omega_{off} = \pm 4kHz$

$$\phi_{BSS} = \frac{B_1^2 \gamma^2}{\omega_{off}} \int_0^T S(t)^2 \, dt$$

where B_1 is the peak amplitude, γ the gyromagnetic ratio and S(t) is the shape of the Bloch-Siegert pulse.

BSS being a phase-based B_1^+ mapping method, it exhibits less sensitivity to relaxation parameters and TR compared to magnitude-based methods. However, the BSS method may suffer from other undesired sensitivity, such as to off-resonance frequency. Another downside of this method is potentially high SAR because of the high-power and relatively long pulses, especially when adiabatic pulses are used.
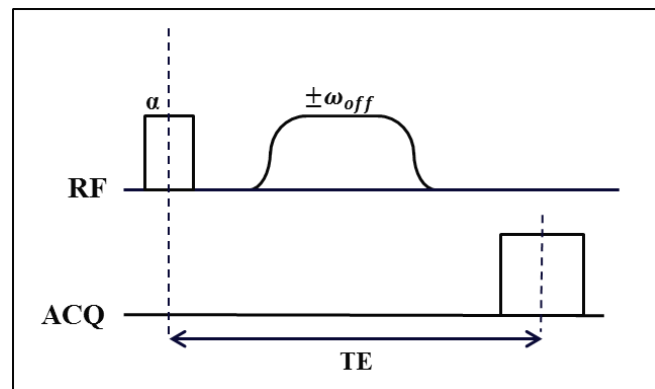
Figure 1.19: Bloch-Siegert shift method pulse sequence diagram: The BSS method employs a GRE pulse sequence with an additional BSS pulse as shown by this pulse sequence diagram.

The Dual Refocusing Echo Acquisition Mode (DREAM) sequence

The Dual Refocusing Echo Acquisition Mode (DREAM) sequence proposed by Nehrke et al. [55] is divided into a stimulated echo preparation period and an acquisition period. Two preparation RF pulses having a flip angle of α are applied during the preparation period. The two alpha pulses are separated by a time interval, TE. A dephaser magnetic field GMC2 is applied between the two alpha pulses. A sequence of reading RF pulses having flip angle β are generated during the acquisition period, temporally subsequent to the preparation period. An

FID signal (I_1) and stimulated echo (STE) signal (I_2) are acquired after each reading pulse as gradient-recalled echoes.

Depending on how the time interval TE is selected, the DREAM approach can offer three timing scheme options, the so-called STE first, FID first and the virtual stimulated echo scheme (STE*). In this work, only the virtual stimulated echo scheme (STE*) that represents the complex-conjugated counterpart of the STE will be used because of the T_2 and T_2* compensation feature of this sequence version [56].
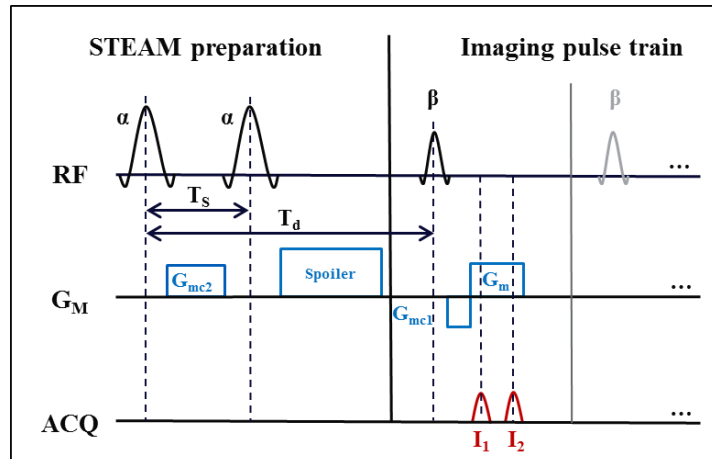
Figure 1.20: DREAM pulse sequence scheme. For clarity slice selection and phase encoding gradients are omitted in this graph.

Directly after the preparation sequence, the longitudinal magnetization is given by:

$$M_{z,STE} = \frac{1}{2} M_0 sin^2(\alpha)$$

$$M_{z,FID} = M_0 cos^2(\alpha)$$

where $M_{z,STE}$ and $M_{z,FID}$ denote the STEAM prepared and unprepared longitudinal magnetization respectively. Neglecting T_1 and T_2 effects, the two acquired GRE signals I_{STE} and I_{FID} are given by:

$$I_{STE} = \frac{1}{2} M_0 \sin(\beta) sin^2(\alpha)$$

$$I_{FID} = M_0 \sin(\beta) cos^2(\alpha)$$

Thus, combining the above equations, the unknown flip angle of the stimulated echo preparation RF pulses, which is proportional to B_1^+, can be derived from the ratio of the acquired echo signals according to:

$$\alpha = \arctan\sqrt{2\, I_{STE}/I_{FID}}$$

Additionally, a B_0 phase map can be generated:

$$arg(I_{FID} \cdot I_{STE}^*) = 2\phi_{B_0}$$

1.4.3. Evaluation of B_1^+ mapping methods for cardiac applications: advantages and limitations

A large number of B_1^+ mapping techniques have been proposed over the course of many years. The most prominent methods were previously examined. They all are able to accurately measure flip angles within a certain range. Each of them is based on different B_1^+ encoding mechanisms. There are many factors influencing the accuracy or practical usefulness of B_1^+ mapping techniques: different number of dimensions, scan time, dynamic range, SAR, off-resonance or B_0 variations and sensitivity to relaxation mechanisms.

Depending on the application, a different B_1^+ mapping technique could be selected. There is still no "Gold-standard" technique. B_1^+ mapping methods are specific sequences that are not directly available on conventional MR systems. Thus, the different methods are implemented on individual research systems and may be difficult to transfer from one scanner to another. Since the DAM relies on the basic GRE and SE sequences, it is always available. For this reason, it is usually used as the method of choice to validate newer techniques [57], [58].

B_1^+ mapping techniques for cardiac or abdominal imaging have the requirement of being fast and simple, providing a viable acquisition window according to physiological motion constrains.

A drawback of most methods is the need for two separate scans to compute a B_1^+ map. This requirement is problematic in MR imaging of the thorax because physiological motion results in phase shifts between successive repetitions of the sequence. This dual repetition necessity leads to erroneous B_1^+ maps. In addition, the time interval between the two separate repetitions may lead to an excessive scan time increase for breath-holding. The need for two separate scans to compute a field map is a disadvantage for cardiac imaging since it requires both scans in the same cardiac phase and respiratory position to obtain reliable field maps. For high field applications, a low SAR is another decisive constrain in selecting a method.

The single-shot characteristic, low SAR and short scan time of the DREAM approach could serve as the optimal method to measure cardiac B_1^+ maps. In general, in thoracic B_1^+ mapping, most methods cannot be used easily because of scan time limitations due to physiological motion.

1.5. Outline

The rest of this thesis is structured as follows:

Chapter 2 introduces the objectives of this thesis work. An alternative B_1^+ mapping method consisting of the three joint approaches is proposed to solve or alleviate the challenges highlighted in chapter 1. Each approach is described here in detail.

Chapter 3 concentrates on the proposed k-space sampling pattern based on the Golden Ratio. This is evaluated by simulating different sampling patterns and retrospectively undersampling and reconstructing an in-vivo dataset. Results showed sharpness improvement with the proposed method in comparison with other sampling patterns for high acceleration factors.

In **Chapter 4,** the proposed B_1^+ mapping method is validated in a static phantom against a gold standard technique, the Bloch-Siegert Shift method and the standard DREAM sequence. Thereafter, this chapter contains a set of phantom experiments to assess the performance of the proposed B_1^+ mapping method and find the optimal imaging parameters for in-vivo applications.

The application and utility of the proposed method is demonstrated in-vivo in **Chapter 5.** Experiments on five healthy subjects were conducted to prove the in vivo feasibility of this approach, applying the optimized parameters found with the previous set of phantom experiments. Variations of B_1^+ values depending on the respiratory state are investigated to evaluate motion-robustness of the proposed B_1^+ mapping method. Reproducibility is also investigated.

Chapter 6 contains a summary of the work presented in this thesis as well as a discussion of possible future research directions

CHAPTER 2

Hypothesis and contribution of this thesis: acquisition and reconstruction framework for an optimal B_1^+ mapping method for cardiac applications

---

The constant motion of the heart imposes particular challenges on cardiac magnetic resonance imaging as compared to MRI of other organs. Cardiovascular MR imaging techniques must meet the challenges of minimizing the effects of cardiac and respiratory motion while providing enough spatial resolution.

Given these concerns, the goal of the present thesis is to develop a B_1^+ mapping method that can be applied in cardiac imaging, with the following requirements:

- The acquisition of a complete B_1^+ map needs to be performed within a small fraction of a second, fitting the diastolic phase of the heartbeat.

- The spatial resolution should be sufficient to study RF uniformities between the different segments of the myocardium.

- Cardiac and respiratory motion should be taken into account, ideally allowing a free breathing acquisition.

Three joint approaches are used in order to adapt the B_1^+ mapping sequence for cardiac applications. Adequate ECG synchronization is the crucial first step in acquiring high quality CMR images. The second approach is an efficient data acquisition strategy. A multi-snapshot undersampling scheme, which relies on the Golden Ratio is used to accelerate the acquisition. Finally, a motion compensated reconstruction algorithm combines these multi-snapshots to compute B_1^+ maps.

2.1. Cardiac gating for the DREAM sequence

Imaging of the heart requires synchronization of the MR signal acquisition to the cardiac cycle, typically by using external sensors to record the heart's electrical activity. This technique is known as cardiac gating.

Prospective synchronization detects the patient physiological signal (R-wave) and after a time called trigger delay (TD), performs the data acquisition. When the next R-wave is detected, this process occurs again until all the data necessary to reconstruct the image is acquired. The TD selects the particular point in the cardiac cycle when the image is acquired. Another parameter called the trigger window represents the percentage of the average cardiac cycle in which acquisitions are not desired (this is generally 10%). These two parameters, TD and TW, allow to calculate the possible length of an MRI acquisition during a cardiac cycle. The trigger delay is set to the beginning of the diastole phase. It is then considered that the heart is

motionless and data acquisition is performed during a fleeting period of relative cardiac quiescence.

2.2. Segmented acquisition of the k-space with a Cartesian sampling pattern based on the Golden Ratio

The DREAM sequence acquires the STE and FID echoes, necessary data to compute a 2D B_1^+ map, in one shot. This is an advantage compared to other methods as DAM [50] or Bloch-Siegert [54] which require separate acquisitions to calculate a B_1^+ map and present higher sensitivity to motion artifacts. Furthermore, a single-shot B_1^+ mapping method requires less time in patient preparation and this benefits not only cardiac applications but also B_1^+ mapping on static body regions.

However, the conventional scan time of DREAM with a high resolution that provides substantial information of the myocardium, is longer than the average diastolic phase of the cardiac cycle. In order to overcome this limitation and reduce the scan time per shot without compromising spatial resolution, the second modification is introduced: a segmented multi-snapshot acquisition with a variable undersampling pattern.

A segmented multi-snapshot acquisition means that the acceleration of the DREAM sequence is achieved by repeating the sequence in the same cardiac phase along several R-R cycles acquiring a certain number of k-space lines within each repetition. Each group of k-space lines, or each time the sequence is performed within a cardiac cycle, is known as snapshot.

In order to optimize the acquisition efficiency, a specific undersampling pattern based on the Golden Ratio is proposed.

Discovered in the ancient Greece, the Golden Ratio (g) is a mathematical proportion that has been studied in many disciples such as nature, art, architecture, botany or finances due to its

interesting properties. The Golden Ratio can be defined by partitioning a line segment, such that the ratio of longer to the shorter partition is equal to the ratio of the initial segment to the longer partition:

$$\frac{a}{b} = \frac{a+b}{a} = g$$

From this equation follows that the Golden Ratio can be determined as the positive root of the quadratic equation:

$$g^2 - g - 1 = 0$$

which is:

$$g = \left(\sqrt{5} + 1\right)/2$$

The Golden Ratio is strongly related to the Fibonacci series as the Golden Ratio is very close to the ratio between two consecutive terms of this well-known sequence F {k}= {1,1,2,3,5...}. It often occurs in nature as in growing patterns of plants, shells and galaxies, and is referred to symmetry of growth, because it allows adding a new element to an already existing arrangement, while preserving the symmetry [59].

In the field of MRI, Winkelmann et al. [60] already applied this mathematical concept to the angle increment between radial projections for time-resolved MRI. That strategy causes radial lines to be very evenly spaced, proving a more efficient acquisition.

For this work, the key idea of the Golden Ratio is introduced in a Cartesian readout. This sampling strategy ensures a uniform distribution of measured data in k-space and enables complementary acquisitions across shots due to the properties of the Golden Ratio.

The analytical expression that describes the k-space undersampling pattern $P(k_y)$ is as follows:

$$P(k_y) = \begin{cases} \left(mod\left(s \cdot i + mod(g \cdot s \cdot (r-1), s)\right), \dfrac{m-Z}{2}\right); & 1 < k_y < \dfrac{m-Z}{2} \\[2ex] \dfrac{m-Z}{2} + j; & \dfrac{m-Z}{2} \le k_y \le \dfrac{m+Z}{2} \\[2ex] \left(mod\left(s \cdot i + mod(g \cdot s \cdot (r-1), s)\right), \dfrac{m-Z}{2}\right) + \dfrac{m+Z}{2}; & \dfrac{m+Z}{2} < k_y < m \end{cases}$$

Where: k_y is the k-space line along the y-direction (phase encode axis); $s(step) = \dfrac{m}{T-Z}$; i=1 to (T-Z)/2; j=1 to Z; m=matrix size; T=Total number of k-space lines acquired; $g = (\sqrt{5}+1)/2$; r=shot number; Z lines around the center of the k-space which are fully acquired in each shot to facilitate motion extraction. In total, T lines (including the Z central lines) are acquired.

After generating the sampling pattern, the profile order is sorted in order to perform a centric acquisition because it minimizes the impact of cardiac motion and this is the optimal profile to reduce systematic errors caused by T_1 relaxation according to earlier studies on the DREAM sequence [56].
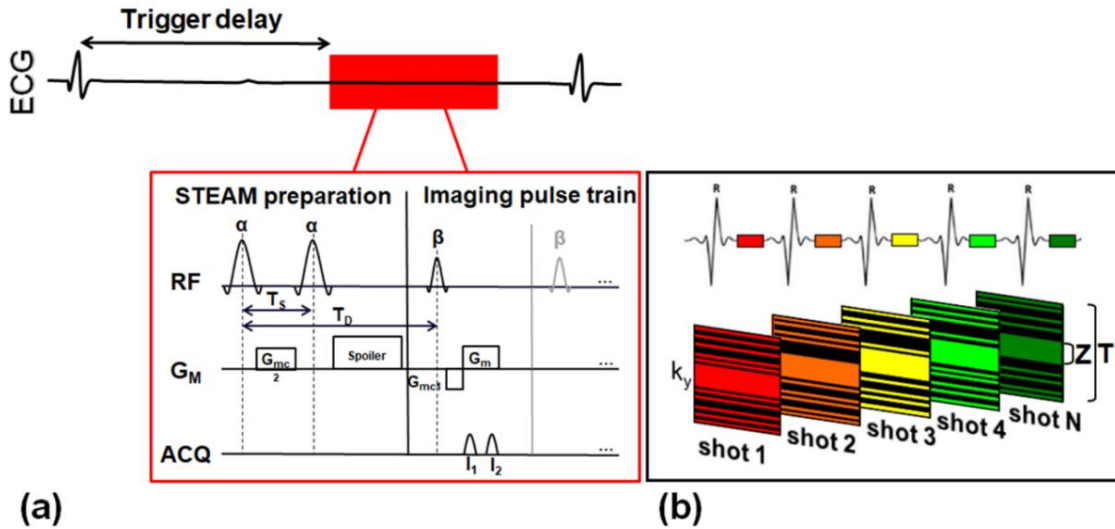
Figure 2.1: *a) Pulse sequence and acquisition scheme for a single shot: the utilized DREAM sequence employs a STEAM preparation consisting of two alpha pulses followed by the imaging pulse train (beta pulses). Acquiring data during diastole is fixed by setting an*

appropriate trigger delay. b) Multi-shot acquisition and undersampling scheme example for Z central lines, T total lines and five shots.

2.3.   Reconstruction framework for Motion Compensation

The STE* and FID echoes required to compute B_1^+ maps with the DREAM sequence are reconstructed following a general joint optimization framework defined as:

$$\rho = \underset{(\rho,\vec{u})}{\mathrm{argmin}}\{\|S - E(\vec{u})\rho\|_2^2 + \lambda\,\psi(\rho)\} \quad with \quad E(\vec{u}) = \zeta F\sigma W(\vec{u})$$

Where the image $\rho \in \mathbb{C}^{n_x \times n_y}$ and the acquired raw data $S \in \mathbb{C}^{n_x \times n_y \times n_r \times n_c}$ with nc the number of receiver coils, and nr de number of shots. Here E is the encoding matrix, $\vec{u}$ represents the displacement fields, ψ is the chosen regularization function, ζ the sampling operator, F the Fourier transform, σ the coil sensitivities weighting, $W(\vec{u})$ the warping operator and $\lambda > 0$ is the corresponding regularization parameter. This optimization problem is solved in three steps similar to the motion compensation strategy described in [41], [61], [62]:

Iterative SENSE reconstruction [62] of each individual undersampled shot. 2) Extraction of in-plane displacement fields in terms of rotational and translational motion between the first shot and all subsequent shots using a non-rigid registration. Note that this process is done separately for the STE* and FID data. 3) Motion compensated joint reconstruction of all STE* data and all FID data, respectively. The different displacement fields from the second step are included into the encoding operator of the iterative SENSE algorithm. Additionally, Tikhonov regularization [63] is used on the gradient of the image to limit noise.

All computations were performed offline using raw k-space data in MATLAB (The Mathworks, Natick, MA, USA).

A schematic representation of the reconstruction steps is shown in figure 2.
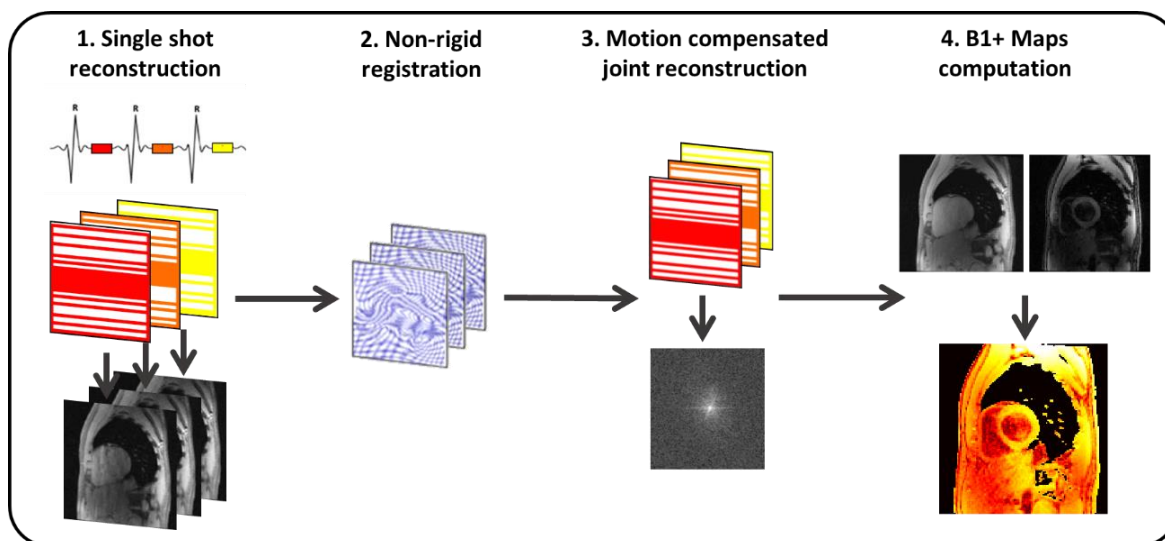
Figure 2.2: *Schematic illustration of the motion compensated reconstruction. Acquisition is performed using complementary trajectories, leading to uniform samplings in the phase encoding direction, which allows for an optimal combination of the k-spaces. The motion model, extracted by non-rigid registration of the images from each shot, is incorporated into the reconstruction process B_1^+ maps are computed after this process is applied to the STE* and FID echoes obtained with the DREAM sequence.*

CHAPTER 3

Study of the k-space sampling pattern[1]

3.1. Introduction

A cquisition strategies define how the k-space is filled with signal data. How signals are acquired into k-space has a direct impact on the spatial, temporal, contrast resolution of the resulting images and scan duration. The order of k-space filling can be manipulated to increase imaging speed to address the inevitable trade-off between scan time and spatial resolution in MRI for cardiovascular applications.

As described in chapter 1.2, motion presents unique challenges and opportunities in MRI. Traditionally, CMR examinations utilize k-space segmentation [64]. This strategy acquires few k-space lines over several cardiac cycles and requires repeated breath-holds and ECG-gating.

---

[1] The content presented in this chapter is based on the conference abstract submitted and presented to the 23rd Annual Scientific Meeting of the ESMRMB 2015, Edinburgh, UK [85].

However, image quality can be degraded by motion artifacts when scanning patients with arrhythmia or poor breath-hold compliance.

In patients who cannot hold their breath for the duration of a segmented acquisition or in whom the ECG signal is weak, a single-shot technique may be used. In contrast to segmented acquisitions, single-shot sequences acquire the complete k-space data required for image reconstruction within a single acquisition window. Such a window is thus placed in between two R-waves. Due to the short acquisition duration of single-shot techniques, such methods tend to be robust against cardiac and breathing motion artifacts. However, the trade-off for increased speed is decreased spatial resolution.

Figure 3.1 shows a clinical case where a segmented late gadolinium enhancement sequence is affected by severe artifacts due to poor breath-holding. Single-shot images clearly showed sub-endocardial enhancement in the septum and anterior wall from mid-cavity to the apex.
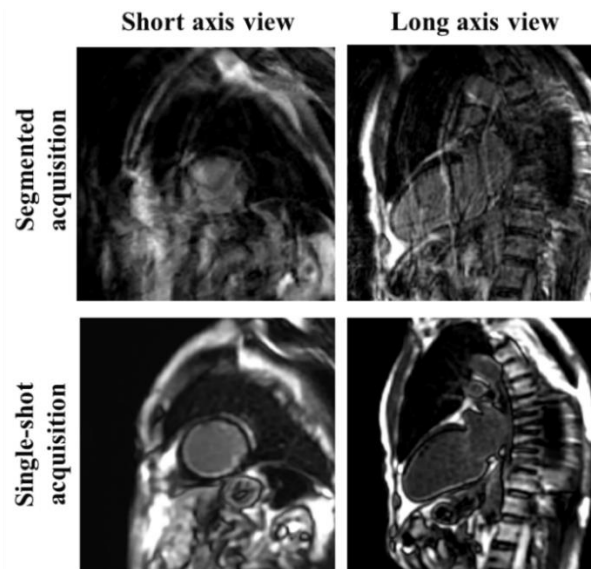
Figure 3.1: Clinical example courtesy of Morriston Hospital, Swansea, UK. Classical segmented Late Gadolinium Enhancement (LGE) sequence presenting severe artifacts due to breath hold difficulties of the patient vs single-shot image.

As explained in chapter 1, section 1.6, MRI presents great flexibility on how to acquire data. By altering the encoding gradients in an appropriate way, one can achieve different trajectories to traverse the k-space. Cartesian, radial, spiral [65] or PROPELLER [66] are only the most common acquisition schemes. Basically, every imaginable trajectory, variation, combination or extension is possible. However, Cartesian k-space sampling forms the vast majority of the present day clinical scans due to the simplicity of image reconstruction and its implementation.

While a lot of tuning of the scanning metrics can be done by manipulating the k-space sampling pattern, another approach is to make use of intrinsic properties of the Fourier domain with dedicated reconstruction techniques. Compressed Sensing (CS; also known as Compressive Sensing or Compressed/Compressive Sampling) [67]–[69] is an advanced mathematical theory used in MRI to reconstruct an image from reduced number of k-space data (undersampled data), greatly reducing scan time. An effective application of CS has three major requirements: i) The image is sparse in some transform domain; ii) the sampling strategy creates incoherent artifacts in case of undersampling. Incoherent in this context means that the artifacts are irregular and indistinguishable from the object, looking like additive random noise; iii) the image is recovered by a non-linear method that enforces both, image sparsity and data consistency [70].

The hypothesis formulated in chapter 2 regarding whether the combination of a single-shot sequence with a sophisticated reconstruction technique could increase the resolution while offering a reduction in scan time and motion artifacts, requires a specific undersampling pattern.

Naturally, the here proposed acquisition scheme is based on these preconditions. In every shot, few lines around the center of k-space are fully acquired while the higher frequencies are undersampled following a variable pattern based on the Golden Ratio.

Hereafter, the impact of the Golden Ratio on the proposed accelerated multi snapshot acquisition strategy is compared to other sampling patterns: random and fixed increment distribution, i.e. equidistant sampling. Figure 3.2 depicts the symmetry of these distributions in one dimension.
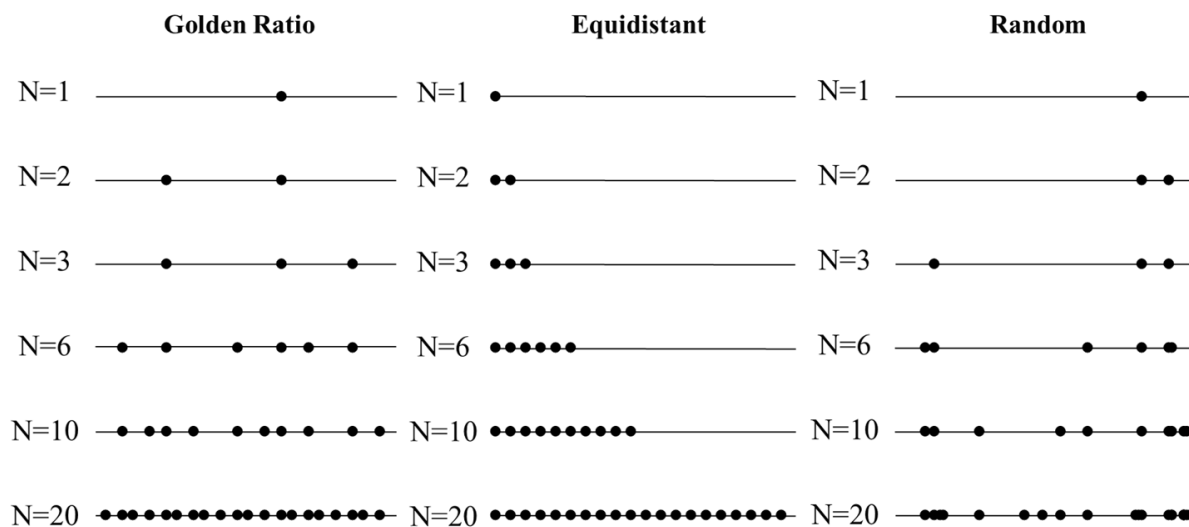
Figure 3.2: *Symmetry of the Golden Ratio sampling compared to a fixed increment distribution (equidistant) and a random distribution. Partitioning is shown for a line segment with n=1,2,3,6,10 and 20 points. In the Golden Ratio distribution, a new point is always placed on one of the largest segments, such that a nearly uniform distribution is attained at all times.*

3.2. Methods

In order to evaluate the impact of the Golden Ratio and the proposed sampling pattern on the reconstruction framework, three different 2D Cartesian k-space filling strategies (equidistant, random and Golden Ratio) were simulated with different degrees of undersampling. The simulation comprises acquisition of a fully sampled dataset followed by retrospective undersampling and reconstruction.

The analytical expression, which describes the proposed k-space undersampling pattern based on the Golden Ratio across shots depending on matrix size, number of shots and other

acquisition parameters, is described in Chapter 2.2. Accordingly, Z=16 lines along the frequency encoding direction, around the center of the k-space were fully acquired in every shot for coil sensitivity calibration and motion extraction. These central lines were simulated not only for the Golden Ratio sampling pattern, but were also incorporated to the equidistant and random sampling patterns for a fair comparison regarding amount of data. Note that this is not typically part of these undersampling methods.

The amount of sampled lines in the phase encoding direction were T= 40,44,48,56 and 64 out of 196. (matrix size 256x256 with a phase FOV= 0.75). This corresponds to the effective acceleration factors, R=3.7; 4.4; 5.5; 6.3 and 7.3.

Imaging was performed on a knee instead of the heart to ensure no motion during the sampling of the whole k-space. Controlled motion was simulated by scanning five different positions imitating a knee extension. In vivo data were acquired on a 3.0T MR750w system (GE Healthcare, WI, USA) using a fast gradient echo (FGRE) sequence. Raw data were exported and reconstructed offline with the reconstruction framework described in Chapter 2.3. Position four, was considered the reference for motion correction. The time needed to run the offline reconstruction for 5 shots was 5 min and 31 seconds on a PC with Intel Core i5 1.9 GHz CPU and 8GB RAM. The overview of the simulation study is illustrated in figure 3.3.
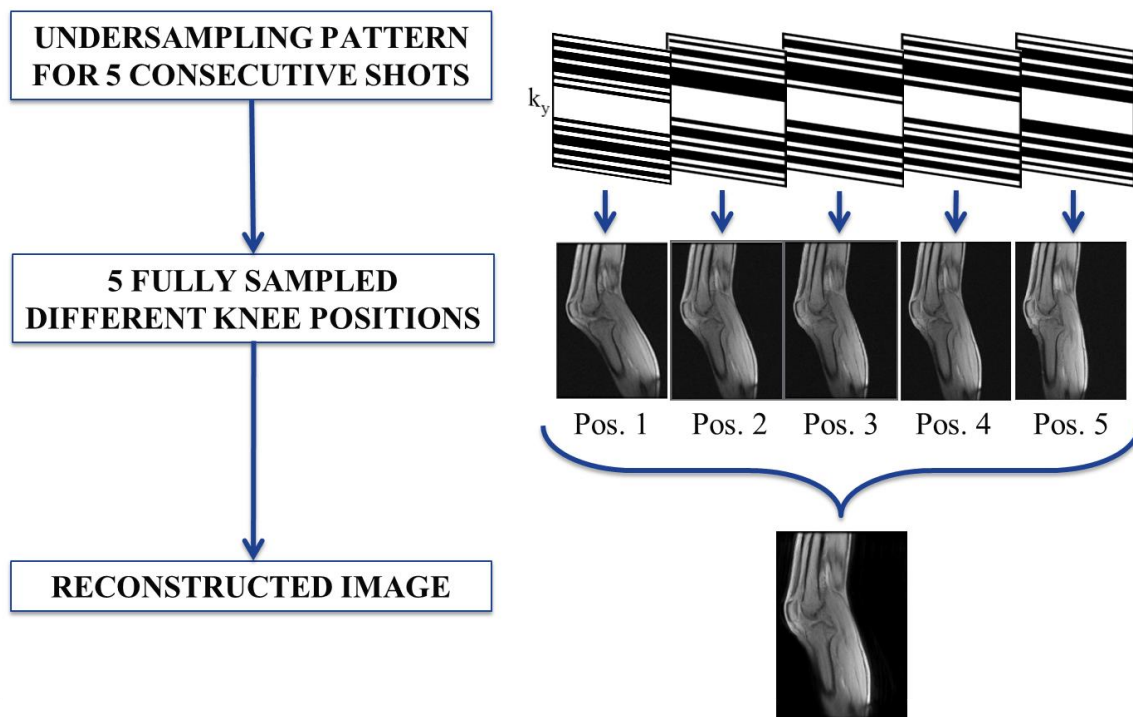
Figure 3.3: *Simulation study overview. White lines indicate acquired lines.*

Reconstructed images were quantitatively analyzed in terms of sharpness and root mean squared error (RMSE). Sharpness measures the variation between the maximum and minimum of signal intensity with a tolerance of 5% along a determined line of pixels where a clear contrast difference was discernible. For each image, using MATLAB software, an intensity profile was measured across the knee muscle to the edge of the tibia, as can be observed in figure 3.4. The local maximum and minimum intensity values across the profile boundary were determined. Next, the distance Δx between $0.05I_{min}$ and $0.05I_{max}$ across this profile was measured and the sharpness value is reported as the slope $(1/\Delta x)$. The sharpness quantization strategy was similar to that used by Shea et al [71].
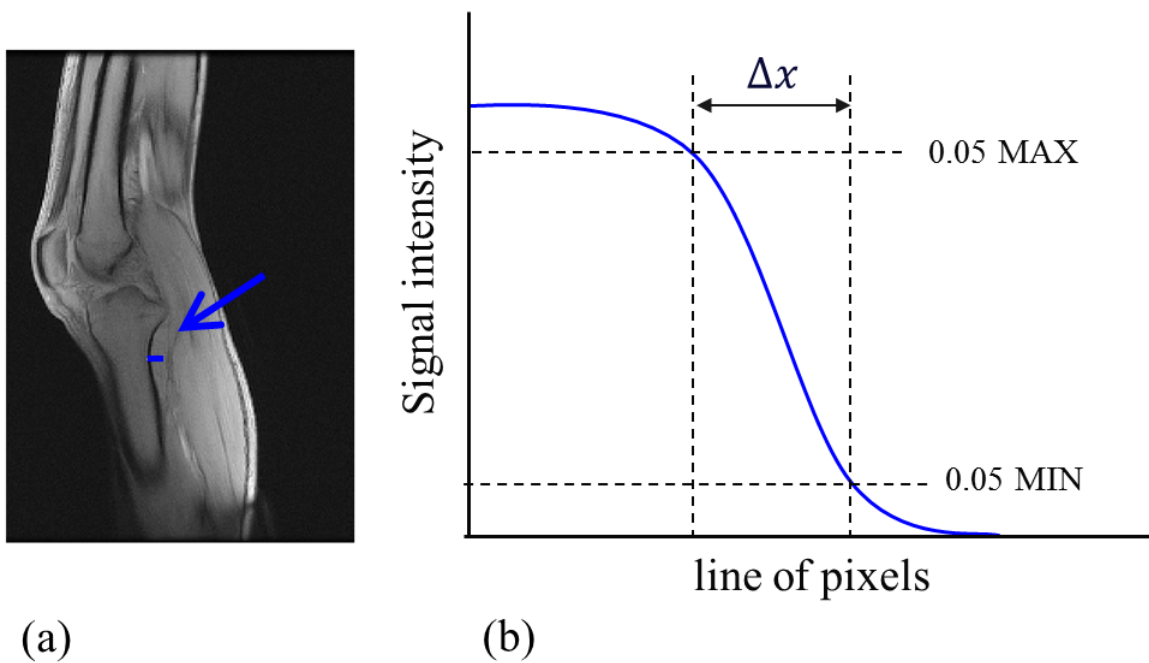
Figure 3.4: *a) Example line drawn across the knee muscle in order to generate a profile for assessment of edge sharpness. b) Diagram showing how sharpness measurements were calculated from the intensity profile. Δx represents the distance between 0.05 maximum and 0.05 minimum intensity values of the profile. The sharpness value is reported as $1/\Delta x$.*

3.3. Results

Figure 3.5 presents the analysis in terms of sharpness and RMSE. Subfigure a) shows the analysis of sharpness with increasing acceleration factors while subfigure b) shows the analysis of the RMSE with increasing acceleration factors. The reference image for these comparisons was the reconstruction of the five fully acquired positions assuming controlled motion between them.
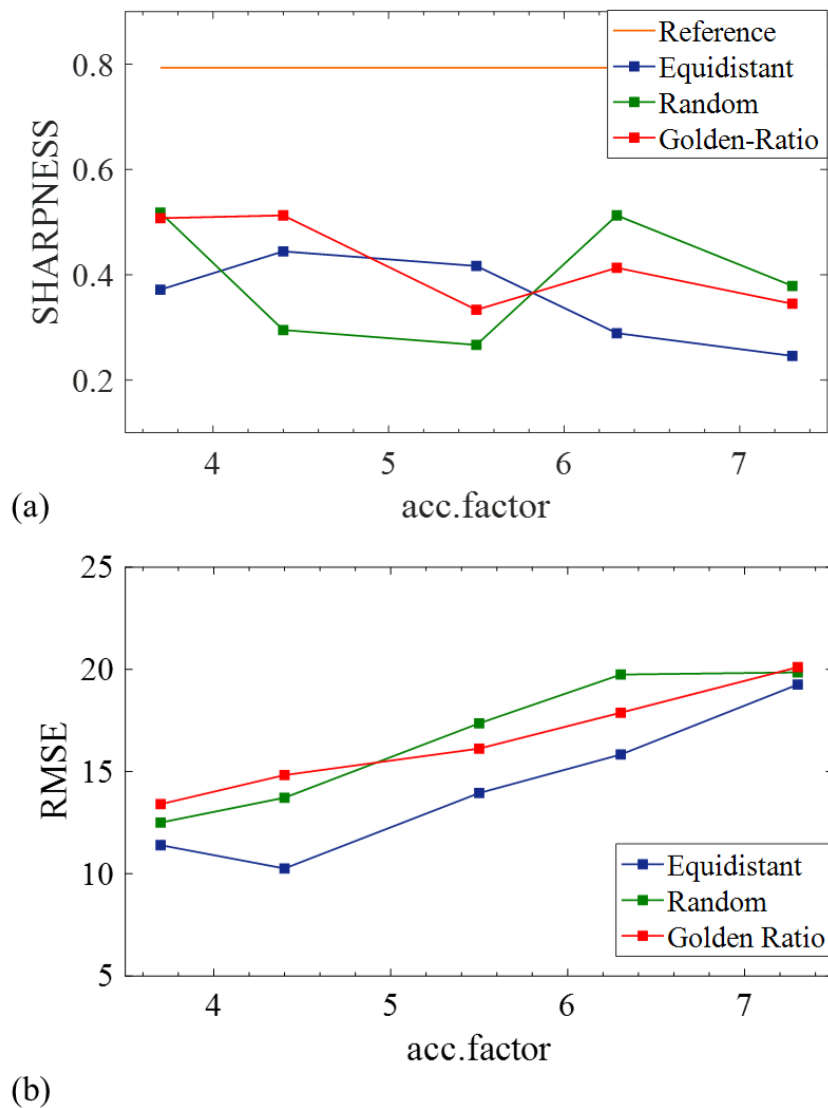
Figure 3.5: *Comparison of undersampling schemes. a) Sharpness vs acceleration factor. b) RMSE vs acceleration factor.*

In general, optimal results are achieved when the number of acquisitions is close to the acceleration factor, this is when a full k-space can be filled assuming complementary acquisitions. This explains why in the RMSE comparison in subfigure 3.5b) using an equidistant plus the central part of k-space sampling presents the lowest RMSE to the reference for an acceleration factor of 4.5. However, weighing up sharpness against RMSE, the Golden

Ratio profile improves image quality clearly in terms of sharpness with higher acceleration factor.

Finally, the Golden Ratio trajectory was also evaluated in vivo in the cardiac region as shown in figure 3.6. Note that the different contrast observed between profiles is due to the different amount of shots.

1-shot   10-shots   **Full acquisition**
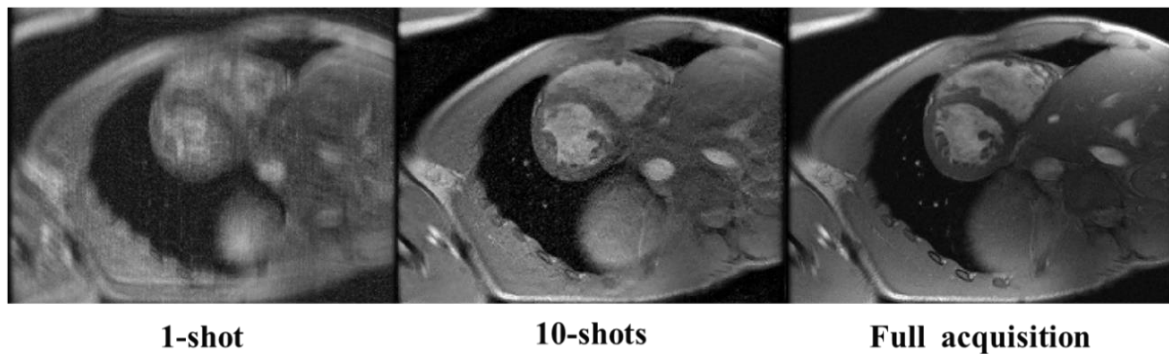
Figure 3.6: *Cardiac short axis reconstruction of a dataset generated from one single-shot and ten single-shots by retrospectively applying the Golden Ratio undersampling pattern with an acceleration factor of R = 3.7 in FGRE acquisitions.*

As demonstrated in figure 3.2, the Golden Ratio undersampling scheme enables an irregular but almost uniform distribution of measured data for any arbitrary number of repetitions, leading to incoherent aliasing. Blurring artifacts can be seen due to the uncollected data in the single-shot reconstruction. However, the combination of ten shots results in similar image quality than a fully sampled acquisition.

3.4. Discussion

The proposed accelerated multi-snapshot acquisition can reconstruct low resolution images from every shot, like single-shot, due to the properties of the undersampling pattern (full acquisition of lower frequencies). The utilized motion correction reconstruction framework, can extract motion from these low-resolution images and obtain higher resolution by

combining multiple acquisitions in free breathing. Thus, equivalent image quality as in conventional breath-hold segmented acquisitions is obtained.

Any sampling strategy that enables complementary acquisitions, meaning that a full k-space can be reconstructed after combining a certain number of shots, could be applied for this acquisition method. A conventional interleaved segmented acquisition performs well for low acceleration factors but as the acceleration factor increases, aliasing artifacts pose the main drawback. According to the CS theory, the lowest coherence in data sampling is achieved with random trajectories. However, random trajectories might generate undesired clusters and larger gaps in the acquired data as illustrated in figure 3.2. These gaps could still generate foldover artifacts due to the non-uniform distribution of energies in the k-space. Moreover, random sampling techniques are computationally inefficient, which is a limiting factor for large scale problems. Thus, variable density undersampling schemes are a better distribution to create incoherent artifacts and at the same time prevent foldover artifacts. One can conclude from the results section that the proposed undersampling scheme based on the Golden Ratio not only presents this property but also performs better compared to the alternative evaluated schemes for high acceleration factors. The proposed approach introduces acquisition flexibility along the phase encoding direction and reduces the acquisition time per shot without compromising spatial resolution.

In theory, a large variety of k-space sampling patterns could potentially be employed for this strategy. However, our study concentrates on 2D Cartesian trajectories for practical considerations. Non-cartesian schemes such as radial or spiral could also be considered since they generate incoherent artifacts. Nevertheless, that case would require a more complex reconstruction framework including additional gridding techniques to transform data onto a Cartesian grid.

CHAPTER 4

Phantom study of the proposed approach

4.1. Introduction

In this chapter, the proposed B_1^+ mapping method was validated in a static phantom against a gold standard technique, the Bloch-Siegert Shift method and the standard DREAM sequence. Thereafter, this chapter contains a set of phantom experiments to assess the performance of the proposed B_1^+ mapping method with the three joint modifications of the DREAM sequence, including the acquisition and reconstruction framework analysed in Chapter 3. The final goal was to find the optimal imaging parameters for in-vivo applications.

4.2. Methods

The proposed method was validated against the Bloch-Siegert Shift method (BSS) [54] in a torso phantom filled with a high conductive liquid. Scans with the proposed DREAM method were acquired with the following imaging parameters: $T_R/T_S/T_D$ = 6.8ms/0.8ms/3.9ms. STEAM flip angle α=60°, imaging flip angle β=15°, matrix size=128x128; FOV(phantom)=460mm; slice thickness=8mm; bandwidth (BW)=31.25kHz. Resulting B_1^+ maps were represented in terms of relative B_1^+ map, which is obtained by dividing the flip

angle map alpha by the nominal flip angle. With the same spatial coverage, the Bloch-Siegert shift method was set up as a 2D GRE sequence with a spiral readout [72]. Two images were acquired to compute the corresponding B_1^+ maps applying a symmetric resonance frequency offset of ±4kHz and a pulse duration of 8ms. A pixel-by-pixel difference in percentage was used for a quantitative comparison of the two methods.

For the second part of this phantom study, the "Eurospin II T05 System Phantom" [73] was used. This phantom comprises twelve tubes with characteristic T_1 and T_2 values. Since it is known that the B_1^+ field smoothly varies across the field of view, the tubes were randomly positioned according to their T_1 and T_2 values. Another spherical phantom was included as a spatial reference to avoid a symmetric setup and B_1^+ maps were obtained using the same scan parameters as for the torso phantom.
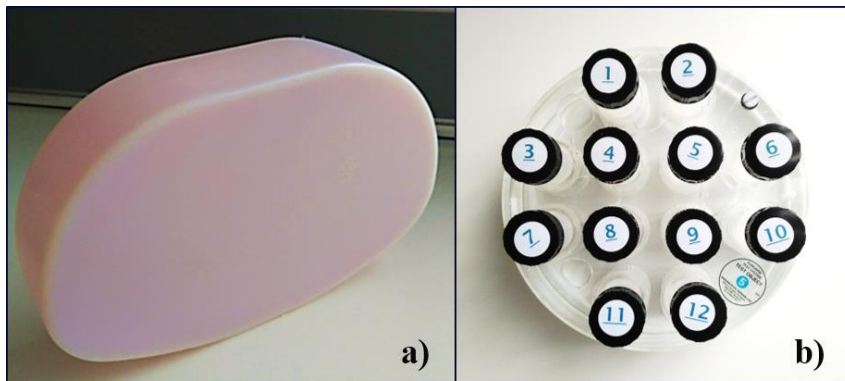
Figure 4.1: a) *Torso phantom b) Eurospin II T05 system phantom.*

T_1 values were calibrated using a 32-points fitting with an inversion recovery spin echo sequence and a regular spin echo sequence for T_2 values. Table 2 shows T_1 and T_2 values for all the tubes.

Tube	T_1 (ms)	T_2 (ms)
1	210	44.1
2	319	61.1
3	323	96.8
4	495	43.5
5	495	78.6
6	451	128.6
7	635	86.6
8	633	121.5
9	799	55.5
10	787	104.7
11	978	70.1
12	1641	99.5
13	1025	122.4
14	1140	70.1
15	1260	90.9
16	1429	128.6
17	1385	122.7

Table 2: *Relaxation times T_1 and T_2 in milliseconds(ms) for the different tubes of the Eurospin II T05 System Phantom.*

Using the Eurospin II T05 System Phantom, the following points were investigated for the modified DREAM sequence:

- Verify that the reconstruction framework is robust to the proposed acquisition scheme and does not introduce artifacts in the B_1^+ maps. For that, B_1^+ maps obtained after a single-shot fully sampled and a multi-shot undersampled acquisition were compared.

- Validate robustness against heart rate. Different ECG signals of 60,75 and 100 beats per minute (bpm) were simulated during the scan of the static phantom to validate robustness of the modified sequence to different time intervals between shots. Considering a non-gated acquisition as reference, relative errors between B_1^+ maps were calculated for each rate.

- Find the appropriate acceleration factor and number of shots to optimize the compromise between scan time and spatial resolution considering that the scan time per shot accepted to acquire data during the diastole phase is about 210 ms for heart rates up to 110bpm [16].

- Evaluate sensitivity to different relaxation times and assess its application for retrospective correction of T_1 and T_2 values.

All experiments were performed on a 3.0T system (GE Healthcare, Milwaukee, WI) using the standard body coil for RF transmission. The body coil is a birdcage volume RF coil consisting of 16 equidistant rungs, 70 cm inner diameter and it is driven by a maximum RF peak output power of 30kW at two feeding ports. The RF phase between these ports is fixed resulting is an elliptical polarized excitation (quadrature mode) without allowing modifications of the B_1^+ field distribution. Signal reception was performed with a 24-channels receive-only torso array. B_0 shimming was applied using the default techniques supplied by the vendor.

4.3. Results

Validation against the Bloch-Siegert Shift (BSS) method

Figure 4.2 shows relative B_1^+ maps acquired with DREAM (a) and BSS (b) for the same axial slice of the torso phantom and the pixel-by-pixel difference (c). The two maps were qualitatively similar in terms of their shape. A mean difference of 3% and a maximum difference of 10% were found when comparing BSS and DREAM, which indicates agreement between the two methods.
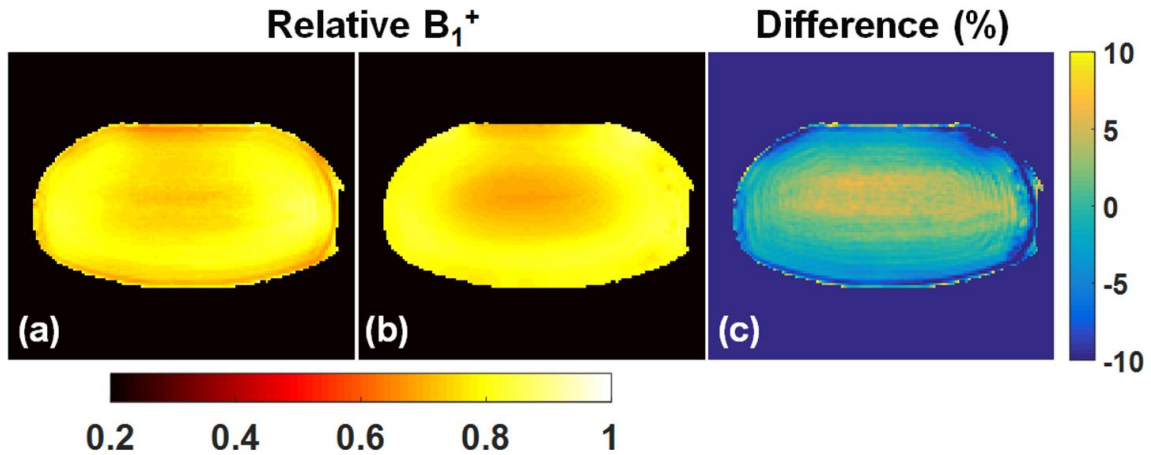
Figure 4.2: *Comparison of relative B_1^+ maps acquired with (a) DREAM and (b) BSS for the same axial slice of the torso phantom. The scale of DREAM and BSS represents the relative B_1^+ values obtained by dividing the flip angle map by the nominal flip angle. (c) DREAM percentage difference with respect to BSS relative B_1^+ maps.*

Validation of the reconstruction framework

Figure 4.3 shows magnitude images of the echoes i.e. FID and STE* and each of the resulting relative B_1^+ maps for a fully sampled single shot, an undersampled single shot and combined multi-shot acquisition. Reconstruction of the individual undersampled shots resulted in blurring. However, images from every shot have sufficient quality to further extract motion fields for in vivo imaging and undersampling artifacts can be corrected after combining multiple shots. Accordingly, similar B_1^+ maps can be obtained with a relative difference between the combined 20-shot image and the fully sampled single shot under 5%.
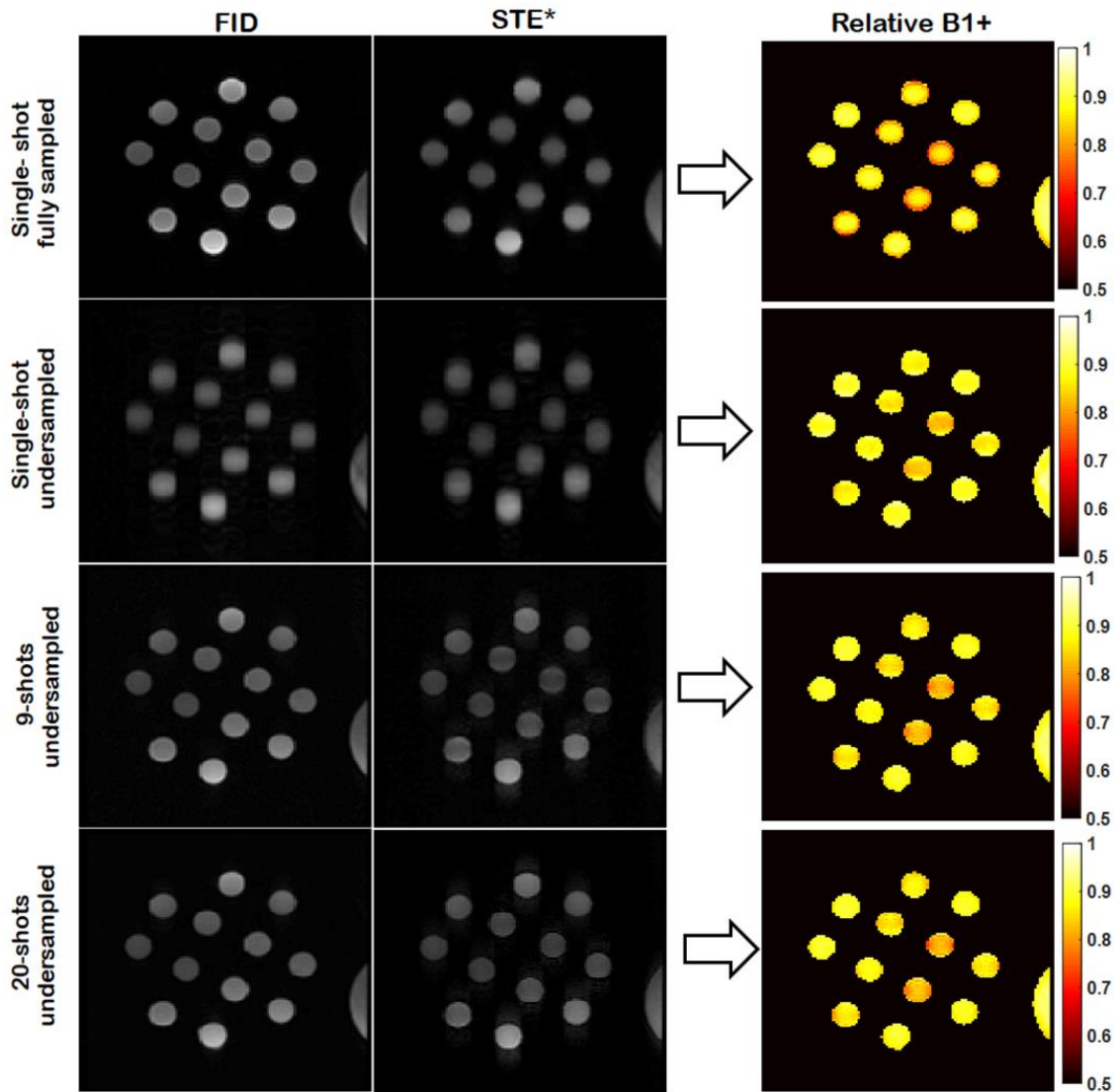
Figure 4.3: *Representative magnitude images of the echoes (FID and STE*) acquired with the proposed method and the resulting relative B_1^+ maps for a single shot fully sampled, undersampled and a combined multi-snapshot acquisition.*

Validation of cardiac gating and robustness to different sampling intervals (heart rate)

The mean relative error between every scan acquired with a simulated ECG signal of 60, 75 and 120 bpm and the reference was lower than 6% across the whole phantom. No dependency on the heart rate value was observed, demonstrating the robustness of the method to different time intervals between shots.

Acceleration factor and number of shots

The proposed undersampling scheme significantly reduces the scan time per shot. The acquisition time for a single shot fully sampled with a 128x128 matrix size was 871ms while in the undersampled case, this time was 218ms. In total, T=32 k-space lines out of 128 were acquired in each shot, where Z=16 lines were fully sampled around the center of the k-space. Z=16 is the minimum amount of lines required to reconstruct a low-resolution image from which motion can be extracted and fed to the reconstruction framework. This distribution resulted in an acceleration factor of seven in the outer k-space and a total effective acceleration factor of four. The undersampling ratio (Z and T) was chosen as a compromise to the scan time requirements for the synchronization with the cardiac cycle, to perform data acquisition during the diastole phase.

Regarding the number of shots, figure 4.4 shows the root mean square error (RMSE) of B_1^+ maps reconstructed after a n-shots undersampled combination, with n=1 to n=20 in comparison to a fully sampled single-shot. Eight shots were determined as the optimal number of shots as the RMSE curve flattened from that number of shots onwards.
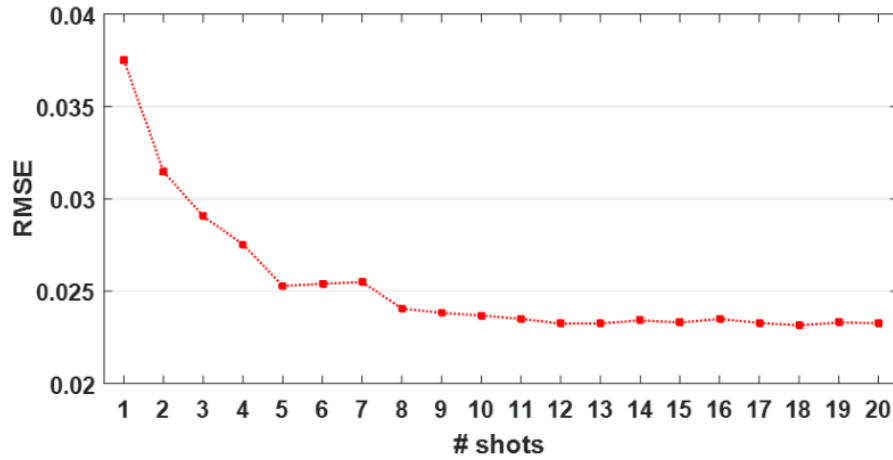
Figure 4.4: *Root mean square error (RMSE) of B_1^+ values computed with n undersampled shots (n from 1 to 20) vs. a single-shot full sampling. RMSE units are in relative B_1^+.*

<u>*T_1 and T_2 dependence*</u>

Figure 4.5 compares the mean relative B_1^+ values within each vial to their T_1 and T_2 values to evaluate T_1 and T_2 weighting effects. Ideally, a B_1^+ mapping method should depend only on the spatial location of the tube and T_1 and T_2 values should not have an impact on the measurements. However, as described in [55], the DREAM approach has a T_1 dependence due to the elaborated timing scheme of the dual refocusing echo, insensitive against susceptibility and chemical shift effects. This dependency for short T_1 values (<500ms) was observed in Figure 4.5a. Nevertheless, myocardial T_1 values at 3.0T are in the range of 965 - 1340ms [19] and, the B_1^+ values in cardiac scans are expected to be stable.

Figure 4.5b shows a negligible impact of T_2 on B_1^+ values. This result represents an experimental validation for the T_2^* compensation of the DREAM mode chosen (STE* first) and is in good agreement with previous studies [56].
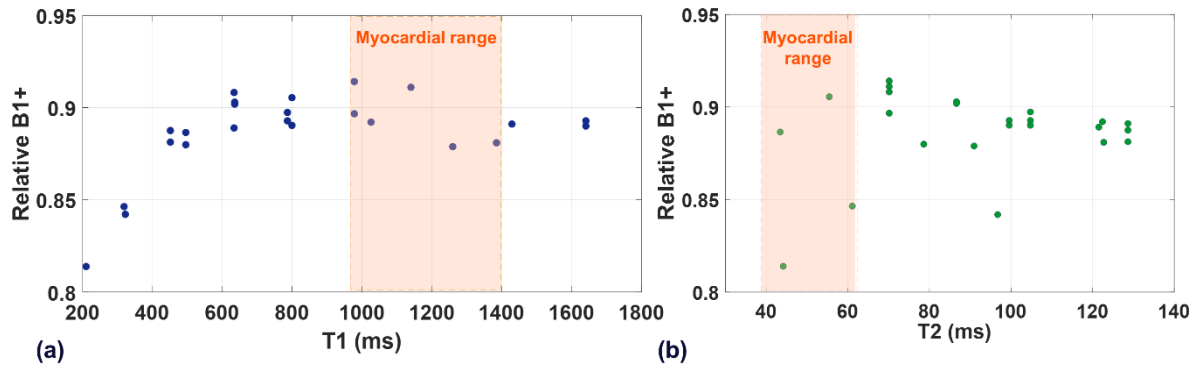
Figure 4.5: *Relative B_1^+ values vs. T_1 (a) and T_2 (b) of the different vials. The vials were placed in a randomized order across the field of view. Myocardial T_1 (965-1394ms) and T_2 (36-59ms) ranges are shown as a reference.*

4.4. Discussion

The comparison between the modified DREAM sequence and the Bloch-Siegert Shift method demonstrates good agreement between the two methods. Since the dielectric properties and phantom geometry were the same, the minimum differences observed could indicate that each technique has slightly different sensitivity to relaxation-time related mechanisms [74] or effects due to the different acquisition schemes.

The undersampling ratio, described in chapter 2 in terms of Z and T, was chosen as a compromise to the scan time requirements for the synchronization with the cardiac cycle. For this undersampling ratio and the scan parameters used in this study, the optimal number of shots required to combine was found to be eight.

Using the Bloch equations, the time delay between the STEAM preparation and the imaging train of the DREAM sequence results in a recovery of the longitudinal magnetization of the FID signal and a decay of the STEAM magnetization [55]. The centric profile ordering minimizes this T_1 weighting effect as it reduces the effective time delay between the STEAM preparation and the imaging sequence. However, it can be observed in Figure 4.5a that the

measured B_1^+ values still have a T_1 dependence, which is significantly pronounced for short T_1. This effect does not pose a problem for regions with relative long T_1. For example, myocardial T_1 values at 3.0T are in the range of 965 - 1340ms. Hence, the B_1^+ values obtained in vivo with the proposed method are expected to be stable and could potentially be used for post-correction of quantitative measurements in the myocardium.

This method is not restricted to cardiac imaging and could benefit other MR-modalities like brain imaging where T_1 values are in the range of 1000ms at 3.0T or higher field strengths where tissues have higher T_1 values. Additionally, to overcome the problem of T_1-relaxation, one could consider reducing the acquisition train duration which can be achieved by increasing the acceleration factor or decreasing the matrix size.

In conclusion, the presented phantom study demonstrated that B_1^+ maps obtained with the proposed acquisition and reconstruction approaches were reliable and robust against different time intervals between shots (different heart rate).

CHAPTER 5

In vivo study of the proposed approach[2]

5.1. Introduction

This chapter presents and discusses the results of a volunteer study to demonstrate the feasibility of the B_1^+ mapping method proposed along this thesis.

5.2. Methods

Experiments on five healthy subjects (age=30±3 years, heart rate=55±12 bpm) were conducted applying the optimized parameters found with the set of phantom experiments described in

---

[2] The content of this chapter is accepted for publication in the Journal of Magnetic Resonance Imaging (JMRI), entitled "*Accelerated Multi-Snapshot Free-Breathing B_1^+ Mapping Based on the Dual Refocusing Echo Acquistion Mode Technique (DREAM): An Alternative to Measure RF Nonuniformity for Cardiac MRI*" and was presented in part at the 25th Annual Meeting of ISMRM. Honolulu; 2017; abstract 3911

chapter 4. One of these was repeated five times in separate breath-holds and five times in free-breathing to investigate repeatability. Informed consent was obtained from each subject and the imaging protocol was reviewed and approved by our Institutional Review Board.

An initial 2D steady-state free precession (SSFP) cine sequence with 30 cardiac phases was acquired to identify the diastolic phase for each volunteer. B_1^+ maps were obtained for one short axis slice. Prospective ECG-gating allowed for imaging during the diastolic phase by setting a trigger delay according to the cine images.

Variations of B_1^+ values depending on the respiratory state were investigated. For this purpose, the proposed DREAM sequence was performed with ECG-gating in free breathing and breath-hold positions (inhale and exhale).

Mean values and standard deviations (STD) of the relative B_1^+ maps were computed within six standardized ROIs on the myocardium according to the American Heart Association (AHA) definition [25]. The six ROIs were outlined on the DREAM magnitude images. The STD and the coefficient of variation (CV) were calculated for the repeatability study. Expressed as a percentage, the CV is the ratio of the standard deviation and the overall mean for all measurements.

5.3. Results

Figure 5.1 shows the relative B_1^+ maps obtained using the proposed method and the spiral Bloch-Siegert sequence in breath-hold for the same short axis view. Equivalent values across the myocardium can be obtained with the two methods with a mean difference of 6%. The blood pool and fat regions were excluded for this comparison due to the sensitivity of the DREAM sequence to flow and short T1 values. Some artifacts due to the spiral readout can be observed on the Bloch-Siegert B_1^+ map as indicated by the arrow.
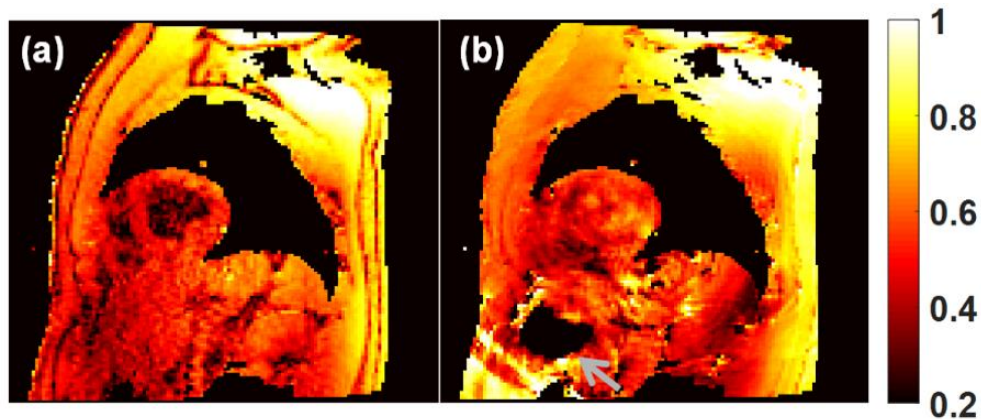
Figure 5.1: *a) Cardiac B_1^+ map obtained with the proposed DREAM sequence for a short axis slice in breath-hold. b) spiral Bloch-Siegert B_1^+ map obtained for the same slice in breath-hold and ECG-gating. The grey arrow at the bottom-left corner indicates spiral artifacts.*

Figure 5.2 depicts relative B_1^+ maps for one representative volunteer using the proposed method in a short axis view for different respiratory states, i.e. inhale, exhale and free breathing after motion correction, respectively. An anatomical reference image acquired with a SSFP cine sequence is shown to facilitate the identification of the myocardium. Figure 5.2 b) shows the mean relative B_1^+ value for each myocardial segment and all volunteers in the free-breathing state.
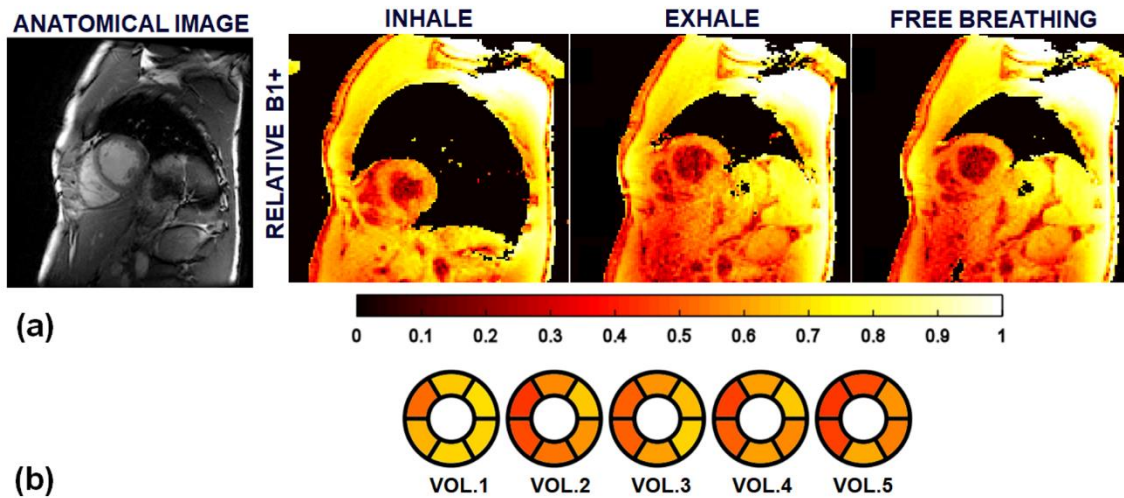
Figure 5.2: a) Anatomical image acquired with a cine sequence at the trigger delay used for DREAM in the diastolic phase for a short axis view of the heart at 3.0T of a representative volunteer and corresponding relative B_1^+ field maps in different respiratory states (inhale, exhale and free-breathing). Standardized representation of the mean relative B_1^+ value for the six myocardial segments and the five volunteers in the free-breathing state. The B_1^+ value varies noticeably in the anteroseptal/anterolateral direction for all volunteers.

Figure 5.3 a) shows the mean and standard deviations of relative B_1^+ values vs respiratory states of a representative volunteer and b) all subjects measured at six ROI in the myocardium. 5.3 a) also indicates the color code used for each ROI location/ myocardial segment. The RF field inside the subject is dependent on the individual subject's anatomy. However, one can observe a similar pattern of field homogeneity across the short axis slice used in this study for all volunteers. The largest variations appear along the anteroseptal/anterolateral direction on the left ventricle wall. The relative B_1^+ value drops from the anteroseptal segment (6) to the anterolateral segment (2) down by 26%. This result is in good agreement with previous work [57] and could be also considered as a quantitative validation of the proposed method. High consistency of B_1^+ values between the free-breathing and breath-hold (inhale/exhale) states indicates the motion robustness of this approach.
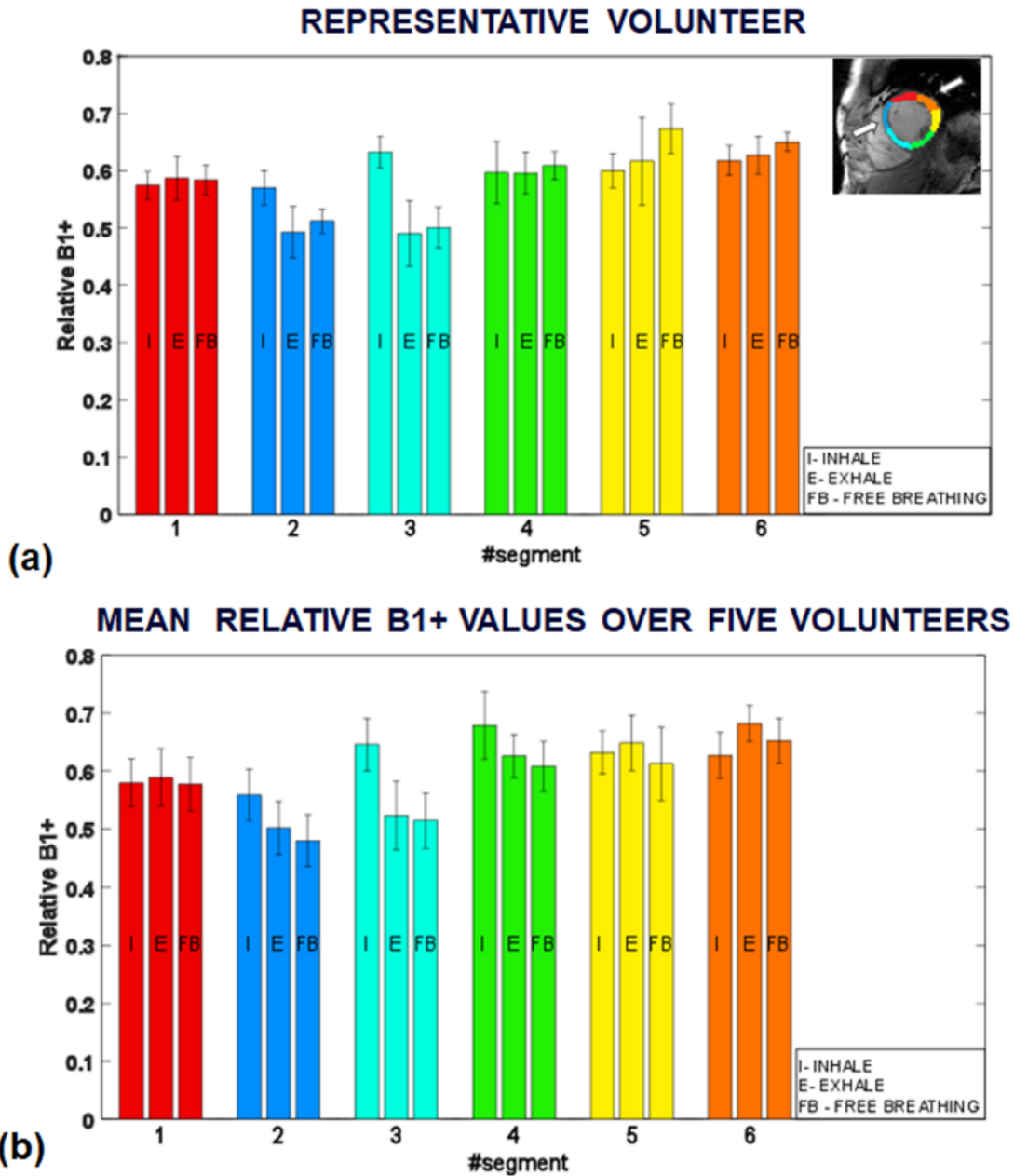
Figure 5.3: *a) Analysis of relative B_1^+ variations vs breathing positions (inhale, exhale and free-breathing) in the six regions of interest (ROIs) for one representative volunteer. b) Mean values across the five volunteers. Color code defined for each segment (ROI). Arrows show anterolateral (6) and anteroseptal (2) segments.*

	Breathhold			Free Breathing		
Segment	B1 Range	STD	CV	B1 Range	STD	CV
1	0.41-0.47	0.03	6%	0.51-0.54	0.01	2%
2	0.39-0.41	0.01	2%	0.44-0.51	0.03	6%
3	0.43-0.48	0.03	5%	0.39-0.43	0.02	5 %
4	0.52-0.56	0.02	3%	0.41-0.53	0.04	9 %
5	0.53-0.58	0.02	4%	0.40-0.52	0.05	10%
6	0.53-0.62	0.04	6%	0.59-0.70	0.04	6%

Table 3: Repeatability results in terms of standard deviation (STD) and coefficient of variation (CV) for each myocardial segment of one volunteer scanned five times in breath-hold in and five times free breathing using the proposed B_1^+ mapping approach.

5.4. Discussion

We have demonstrated the feasibility of a cardiac gated multi-snapshot B_1^+ mapping approach, which was tested here at 3.0T but could be transferred to a higher or lower field strength. This method allows for motion compensated B_1^+ mapping, leading to reproducible B_1^+ maps in the myocardium.

Previous studies that compare and evaluate the performance of the existing techniques to map the B_1^+ field [74], [75], reported on the standard DREAM sequence as a validated method with the advantages described hereinafter. Single-shot sequences are favorable for fast imaging applications to address intra-acquisition motion. Other B_1^+ mapping methods, such as the conventional Double Angle Method or Bloch-Siegert [52], [54] require two separate acquisitions to compute a B_1^+ map and therefore present higher sensitivity to motion. Hence, the main benefit of the DREAM sequence is that B_1^+ maps can be obtained after one single acquisition, removing any location mismatch between the two acquisitions. Another advantage

of the DREAM sequence is the low flip angle used for imaging, particularly interesting for high field applications due to its low SAR footprint. Additionally, the DREAM approach provides simultaneous B_0 maps. Although studying B_0 changes was beyond the scope of this study, this could be also beneficial for other applications.

Since the scan time of one single-shot with the DREAM sequence exceeds the average diastolic phase of the cardiac cycle, the acquisition efficiency was optimized by performing a segmented multi-snapshot acquisition with a variable undersampling pattern based on the Golden Ratio. The scan time per shot was reduced by a factor of 4 compared to a fully sampled single shot. This minimizes cardiac motion and introduces acquisition flexibility along the phase encoding direction, reducing the acquisition time per shot without compromising spatial resolution.

The motion compensated reconstruction framework enables free-breathing acquisition, improving patient comfort and workflow. This could have a significative impact on B_1^+ shimming in combination with multi-transmit systems. To determine the shim components, a B_1^+ map needs to be acquired for each RF channel. With other methods, one can acquire 2 B_1^+ maps for a 2-channel system in a single breath-hold [76], while the free-breathing aspect of the presented approach could allow measuring B_1^+ maps for systems with more than 2 channels.

Another benefit of the proposed method is the SPGR Cartesian k-space readout, commonly used in clinical MR sequences. Reconstructions from Cartesian sampling are robust to many sources of system imperfections. Hence, this simplifies image processing as it relies on standard reconstruction techniques available in most MRI systems. This may simplify a potential integration into the clinical workflow, considering that B_1^+ shimming in the heart region is not a standard feature on commercial multi-transmit systems.

However, the STEAM preparation of the DREAM sequence is highly sensitive to flow artifacts. This is the main reason for the contrast between the blood pool and myocardium. In some cases, signal voids due to turbulent flow patterns can be observed as reported also in

previous studies [77]. Thus, the interpretation of the B_1^+ values should be restricted to the myocardium during the diastolic phase of the heart to avoid these artifacts. For this reason, a precise ECG-triggering is essential.
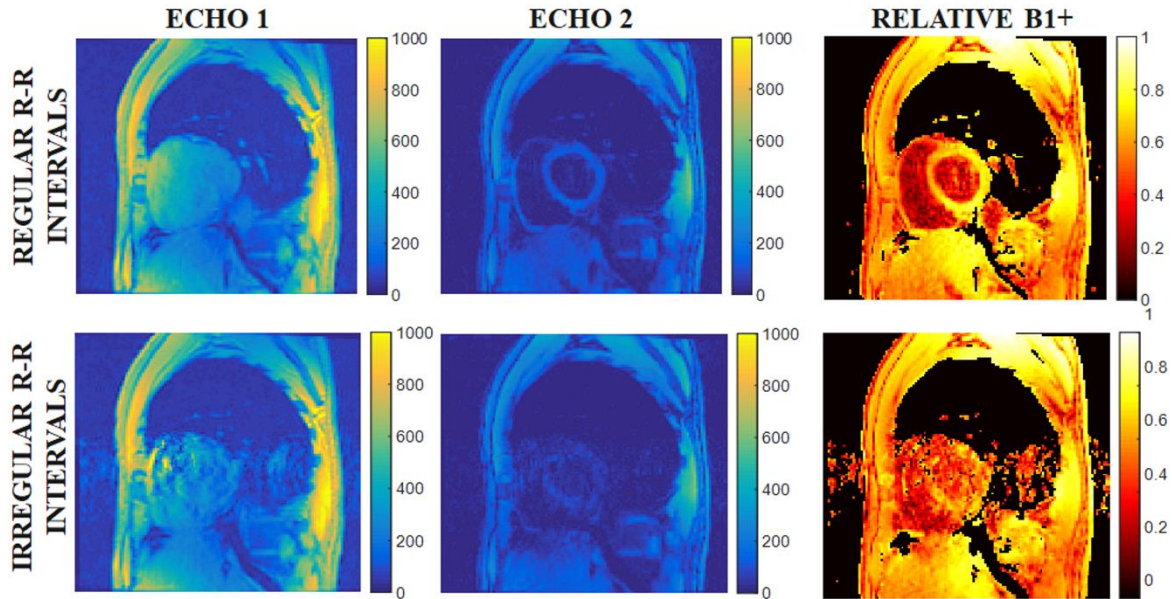
Figure 5.4: *Example of the two echoes and the corresponding B_1^+ map during an acquisition with regular R-R intervals and irregular R-R intervals where artifacts can be observed.*

Another limitation of the method could be potential through-plane motion as the reconstruction framework only compensates for in-plane motion. Nevertheless, assuming a smoothly varying transmitter B_1^+ inhomogeneity, the impact of through-plane motion may be negligible compared to the slice thickness.

The relative B_1^+ variation observed between basal anteroseptal and anterolateral segments was about 26%, which is consistent with prior reports [57] and could be also considered as a quantitative validation of the proposed method. This result was observed on B_1^+ maps obtained after free-breathing and breath-hold acquisitions, which proves the motion-robustness of the presented technique with good repeatability (STD < 0.05).

CHAPTER 6

Conclusions and Future Work

This thesis was motivated by two active research areas in MRI. The first is a consequence of the current push towards higher field imaging. Higher magnetic field ($B_0 \geq 3.0T$) results in stronger RF field inhomogeneities (B_1^+) originated from the electromagnetic interaction between the patient and the field itself. This can lead to shading artifacts and contrast variations, consequently degrading the overall image quality, and thereby compromising the diagnostic value of the images. The second are the intrinsic challenges of MR imaging of moving organs, in particular the human heart.

The main goal of the work presented here was the development of a B_1^+ mapping method that allows for the investigation of spatial homogeneity of the transmitted radiofrequency field in the myocardium at 3.0T. This method should overcome the challenges of cardiovascular magnetic resonance imaging, summarized as the trade-off between acquisition time, resolution and motion artifacts.

This thesis was also driven by the recent development of the Dual Refocusing Echo Acquisition Mode (DREAM) sequence [55]. In contrast to other methods, the two signals required to compute a B_1^+ map are acquired within one acquisition, making this sequence less sensitive to motion. Additionally, the short scan time and low SAR burden make DREAM a promising approach for cardiac B_1^+ mapping specifically at high field strength.

The contribution of this thesis was an efficient free-breathing and motion-robust B_1^+ mapping method. As described in chapter 2, three joint approaches were used to adapt the DREAM sequence for cardiac applications:

- Prospective ECG triggering to synchronize acquisition with the diastolic phase of the cardiac cycle.
- A multi-snapshot undersampling scheme which relies on the Golden Ratio to accelerate the acquisition, reducing the scan time per trigger.
- A motion-compensation reconstruction framework based on low-resolution images acquired in each snapshot to enable free-breathing and motion-robust acquisition without compromising spatial resolution.

As analyzed in chapter 3, the sampling pattern based on the Golden Ratio introduces acquisition flexibility along the phase encoding direction and reduces the acquisition time per shot without compromising spatial resolution. This acquisition strategy showed better performance compared to other undersampling schemes especially when high acceleration factors were used.

In chapter 4 the proposed method was compared to a gold standard method, the Bloch-Siegert Shift. Phantom experiments indicated good agreement between the two methods (mean difference=3%). This phantom study also showed that the proposed reconstruction approach was reliable and robust against different time intervals between shots (different heart rate).

Finally, (in chapter 5,) the in vivo feasibility was shown in five healthy volunteers. Equivalent B_1^+ distributions for free-breathing and breath-hold in vivo experiments demonstrated the motion robustness of this method with good repeatability (STD<0.05).

In vivo experiments were conducted only as a proof of concept. A direct continuation of this work would be further investigation of the B_1^+ field distribution on different cardiac planes. However, there are still several aspects of this work that are susceptible to improvement and could represent future research opportunities.

- It would be interesting to extend this work to assess its applicability in patients where motion is more challenging, such as patients suffering from irregular cardiac cycles. An arrhythmia rejection algorithm could be integrated into the acquisition software. Thus, data obtained during R-R intervals that are out of a certain range would be discarded and scanned again. Another improvement in cardiac gating for ultra-high field imaging might be replacing ECG by other triggering strategy less sensitive to the magnetohydrodynamic field effect. Some alternatives are described in chapter 1, section 2.3.

- As discussed in chapter 5, one of the disadvantages of the DREAM sequence is the STEAM preparation and its high sensitivity to flow artifacts. Further work to obtain reliable B_1^+ values not only in the muscle tissue and the myocardium but also in the blood pool, could be the implementation of flow compensation or reconstruction by projection into a spherical-function as has been suggested by [78]. Such approach derives a model of the B_1^+ distribution from areas with reliable values and extrapolates to regions where the signal is missing or corrupted due to artifacts.

- This study was conducted with a single body coil transmission in conjunction with a multi-channel surface receiver coil, which is also the standard hardware in clinical systems. Nevertheless, the B_1^+ mapping method proposed here is not limited to this

setup and could be employed to assess the performance of multi-channel surface RF coil transmission for cardiac MR. This configuration has been reported by [79] as an alternative to enhance B_1^+ homogeneity, improve the transmit efficiency by facilitating shorter repetition times and could be beneficial especially for patients with implants since RF power deposition is limited to a specific body region. Despite the many benefits offered by parallel transmission [80], [81], its wide clinical adoption is still hindered by the significant time penalty required to calibrate all the transmit channels.

To conclude, prior knowledge of the transmitted RF uniformity could potentially benefit applications such as B_1^+ shimming or quantitative imaging applications [49] and could have a significant impact on clinical outcome, especially at high fields. Additionally, B_1^+ mapping is also a tool which can be used not only in cardiac MRI but also in other applications such as spectroscopy [82] and may be used to determine electrical tissue parameters [83] or predict SAR [84] in a patient-specific manner for different anatomical regions.

SCIENTIFIC CONTRIBUTIONS

Journal Publication

- **Rincón-Domínguez T.,** Menini A., Solana A. B., Fischer A., Kudielka G., Haase A., Burschka D. "Accelerated Multi-Snapshot Free-Breathing B1+ Mapping Based on the Dual Refocusing Echo Acquisition Mode Technique (DREAM): An Alternative to Measure RF Nonuniformity for Cardiac MRI". Accepted for publication in the Journal of Magnetic Resonance Imaging (JMRI)". June 2018. DOI: 10.1002/jmri.26234.

Conference Proceedings

- **Rincón T.,** Menini A., Solana A.B., Fischer A., Kudielka G., Sun W. "Free breathing Motion-Robust Cardiac B1+ mapping at 3.0T based on DREAM". ISMRM 25th Annual Meeting & Exhibition. April 2017, Honolulu, USA.

- **Rincón T.,** Menini A., Solana A.B., Fischer A., Kudielka G., Sun W. "Free breathing Motion-Robust Cardiac RF Field mapping for MRI". Marie Curie Alumni Association General Assembly. March 2017, Salamanca, Spain.

- **Rincón T.,** Menini A., Bustin A., Solana A. B., Janich M. A., Kudielka G., Burschka D., Brau A. "Multiple Accelerated Single Shot Acquisition for Motion Correction in MRI" 32nd Annual Scientific Meeting of ESMRMB October 2015, Edinburgh, United Kingdom.

- Bustin A., Menini A., Liu S., **Rincón T.,** Burschka D., Janich M., Wolff S., Shubayev O., Stanley D., Odille F, Brau A. "Motion Compensated Reconstruction in Accelerated Single-Shot Cardiac MRI". ISMRM 23th Annual Meeting & Exhibition. June 2015, Toronto, Canada.

- Bustin A., Menini A., **Rincón T**., Liu S., Burschka D., Janich M., Wolff S., Shubayev O., Stanley D., Odille F., Brau A. "Reconstruction avec Compensation de Mouvement en IRM Cardiaque Single-Shot". Proceedings of the Annual Meeting of SFRMBM. March 2015, Grenoble, France.

LIST OF FIGURES

References for illustrations of other publications or internet:

- **Figure 1.3b:** Adapted from Plein, S., Greenwood, J., & Ridgway, J. P. (2011). Cardiovascular MR Manual. https://doi.org/10.1007/978-1-84996-362-6.

- **Figure 1.10:** See page for author [GFDL http://www.gnu.org/copyleft/fdl.html or CC-BY--SA-3.0 (http://creativecommons.org/licenses/by-sa/3.0/)] -Wikimedia Commons.

- **Figure 1.11**: DanielChangMD revised original work of DestinyQx – Wikimedia Commons.

- **Figure 1.12:** Adapted from http://www.vhlab.umn.edu/atlas/cardiac-mri/index.shtml

- **Figure 1.13:** Adapted from [25] - M. D. Cerqueira, N. J. Weissman, V. Dilsizian, A. K. Jacobs, S. Kaul, W. K. Laskey, D. J. Pennell, J. A. Rumberger, T. Ryan, M. S. Verani, and M. S. American Heart Association Writing Group on Myocardial Segmentation and Registration for Cardiac Imaging, "Standardized myocardial segmentation and nomenclature for tomographic imaging of the heart. A statement for healthcare professionals from the Cardiac Imaging Committee of the Council on Clinical Cardiology of the American Heart Association.," *Circulation*, vol. 105, no. 4, pp. 539–42, Jan. 2002.

BIBLIOGRAPHY

[1]   F. Bloch, W. W. Hansen, and M. Packard, "The Nuclear Induction Experiment," *Phys. Rev.*, vol. 70, no. 7–8, pp. 474–485, Oct. 1946.

[2]   E. M. Purcell, H. C. Torrey, and R. V. Pound, "Resonance Absorption by Nuclear Magnetic Moments in a Solid," *Phys. Rev.*, vol. 69, no. 1–2, pp. 37–38, Jan. 1946.

[3]   R. Damadian, "Tumor Detection by Nuclear Magnetic Resonance," *Science (80-.).*, vol. 171, no. 3976, pp. 1151–1153, Mar. 1971.

[4]   P. C. Lauterbur, "Image Formation by Induced Local Interactions: Examples Employing Nuclear Magnetic Resonance," *Nature*, vol. 242, no. 5394, pp. 190–191, Mar. 1973.

[5]   P. Mansfield and P. K. Grannell, "NMR 'diffraction' in solids?," *J. Phys. C Solid State Phys.*, vol. 6, no. 22, pp. L422–L426, Nov. 1973.

[6]   P. Mansfield, A. A. Maudsley, and B. Sc, "Medical imaging by NMR," *Br. J. Radiol.*, vol. 50, pp. 188–194, 1977.

[7]   A. Haase, J. Frahm, D. Matthaei, W. Hänicke, and K.-D. Merboldt, "FLASH imaging: Rapid NMR imaging using low flip-angle pulses," *J. Magn. Reson.*, vol. 213, no. 2, pp. 533–541, Dec. 2011.

[8]   P. Mansfield, "Multi-planar image formation using NMR spin echoes," *J. Phys. C Solid State Phys.*, vol. 10, no. 3, pp. L55–L58, Feb. 1977.

[9]   D. Ma, V. Gulani, N. Seiberlich, K. Liu, J. L. Sunshine, J. L. Duerk, and M. A. Griswold, "Magnetic resonance fingerprinting," *Nature*, vol. 495, no. 7440, pp. 187–192, Mar. 2013.

[10] M. A. Bernstein, K. F. King, and X. J. Zhou, *Handbook of MRI pulse sequences*. Academic Press, 2004.

[11] P. T. Callaghan, *Principles of nuclear magnetic resonance microscopy*. Clarendon Press, 1993.

[12] R. W. Brown, Y.-C. N. Cheng, E. M. Haacke, M. R. Thompson, and R. Venkatesan, *Magnetic Resonance Imaging: Physical Principles and Sequence Design, Second Edition.* Chichester, UK: John Wiley & Sons Ltd, 2014.

[13] P. Zeeman, "The Effect of Magnetisation on the Nature of Light Emitted by a Substance," *Nat. 1897 551424*, Feb. 1897.

[14] W. G. Proctor and F. C. Yu, "The Dependence of a Nuclear Magnetic Resonance Frequency upon Chemical Compound," *Phys. Rev.*, vol. 77, no. 5, pp. 717–717, Mar. 1950.

[15] K. N. Hasgall PA, Di Gennaro F, Baumgartner C, Neufeld E, Gosselin MC, Payne D, Klingenböck A, ""IT'IS Database for thermal and electromagnetic parameters of biological tissues" Version 3.0." 2015.

[16] C. L. Garrard, A. M. Weissler, and H. T. Dodge, "The relationship of alterations in systolic time intervals to ejection fraction in patients with cardiac disease.," *Circulation*, vol. 42, no. 3, pp. 455–62, Sep. 1970.

[17] P. et al. Ponikowski, "2016 ESC Guidelines for the diagnosis and treatment of acute and chronic heart failure," *Eur. Heart J.*, vol. 37, no. 27, pp. 2129–2200, Jul. 2016.

[18] O. Bruder, A. Wagner, M. Lombardi, J. Schwitter, A. van Rossum, G. Pilz, D. Nothnagel, H. Steen, S. Petersen, E. Nagel, S. Prasad, J. Schumm, S. Greulich, A. Cagnolo, P. Monney, C. C. Deluigi, T. Dill, H. Frank, G. Sabin, S. Schneider, and H. Mahrholdt, "European Cardiovascular Magnetic Resonance (EuroCMR) registry--multi national results from 57 centers in 15 countries.," *J. Cardiovasc. Magn. Reson.*, vol. 15, no. 1, p. 9, Jan. 2013.

[19] F. von Knobelsdorff-Brenkenhoff, M. Prothmann, M. A. Dieringer, R. Wassmuth, A. Greiser, C. Schwenke, T. Niendorf, and J. Schulz-Menger, "Myocardial T1 and T2 mapping at 3 T: reference values, influencing factors and implications," *J. Cardiovasc.*

Magn. Reson., vol. 15, no. 1, p. 53, Jun. 2013.

[20] S. Fratz, T. Chung, G. F. Greil, M. M. Samyn, A. M. Taylor, E. R. Valsangiacomo Buechel, S.-J. Yoo, and A. J. Powell, "Guidelines and protocols for cardiovascular magnetic resonance in children and adults with congenital heart disease: SCMR expert consensus group on congenital heart disease.," *J. Cardiovasc. Magn. Reson.*, vol. 15, no. 1, p. 51, Jun. 2013.

[21] C. M. Kramer, J. Barkhausen, S. D. Flamm, R. J. Kim, E. Nagel, and Society for Cardiovascular Magnetic Resonance Board of Trustees Task Force on Standardized Protocols, "Standardized cardiovascular magnetic resonance (CMR) protocols 2013 update.," *J. Cardiovasc. Magn. Reson.*, vol. 15, no. 1, p. 91, Oct. 2013.

[22] D. Lin and C. M. Kramer, "Late gadolinium-enhanced cardiac magnetic resonance.," *Curr. Cardiol. Rep.*, vol. 10, no. 1, pp. 72–8, Feb. 2008.

[23] E. B. Schelbert and D. R. Messroghli, "State of the Art: Clinical Applications of Cardiac T1 Mapping," *Radiology*, vol. 278, no. 3, pp. 658–676, Mar. 2016.

[24] R. J. Lederman, "Cardiovascular Interventional Magnetic Resonance Imaging Cardiovascular Interventional Magnetic Resonance Imaging How MRI Creates Images for Intervention," *Circulation*, vol. 112, pp. 3009–3017, 2005.

[25] M. D. Cerqueira, N. J. Weissman, V. Dilsizian, A. K. Jacobs, S. Kaul, W. K. Laskey, D. J. Pennell, J. A. Rumberger, T. Ryan, M. S. Verani, and M. S. American Heart Association Writing Group on Myocardial Segmentation and Registration for Cardiac Imaging, "Standardized myocardial segmentation and nomenclature for tomographic imaging of the heart. A statement for healthcare professionals from the Cardiac Imaging Committee of the Council on Clinical Cardiology of the American Heart Association.," *Circulation*, vol. 105, no. 4, pp. 539–42, Jan. 2002.

[26] M. L. Wood and R. M. Henkelman, "MR image artifacts from periodic motion.," *Med. Phys.*, vol. 12, no. 1985, pp. 143–151, 2013.

[27] A. M. Gharib, D. A. Herzka, A. O. Ustun, M. Y. Desai, J. Locklin, R. I. Pettigrew, and M. Stuber, "Coronary MR angiography at 3T during diastole and systole," *J. Magn. Reson. Imaging*, vol. 26, no. 4, pp. 921–926, Oct. 2007.

[28] W. Yong Kim, M. Stuber, K. V. Kissinger, N. T. Andersen, W. J. Manning, and R. M. Botnar, "Impact of bulk cardiac motion on right coronary MR angiography and vessel wall imaging," *J. Magn. Reson. Imaging*, vol. 14, no. 4, pp. 383–390, 2001.

[29] M. Stuber, R. M. Botnar, P. G. Danias, D. K. Sodickson, K. V. Kissinger, M. Van Cauteren, J. De Becker, and W. J. Manning, "Double-oblique free-breathing high resolution three-dimensional coronary magnetic resonance angiography," *J. Am. Coll. Cardiol.*, vol. 34, no. 2, pp. 524–531, Aug. 1999.

[30] Y. Wang, E. Vidan, and G. W. Bergman, "Cardiac Motion of Coronary Arteries: Variability in the Rest Period and Implications for Coronary MR Angiography," *Radiology*, vol. 213, no. 3, pp. 751–758, Dec. 1999.

[31] J. Krug, G. Rose, D. Stucht, G. Clifford, and J. Oster, "Limitations of VCG based gating methods in ultra high field cardiac MRI," *J. Cardiovasc. Magn. Reson.*, vol. 15, no. Suppl 1, p. W19, Jan. 2013.

[32] T. Frauenrath, F. Hezel, W. Renz, T. d'Orth, M. Dieringer, F. von Knobelsdorff-Brenkenhoff, M. Prothmann, J. Menger, and T. Niendorf, "Acoustic cardiac triggering: a practical solution for synchronization and gating of cardiovascular magnetic resonance at 7 Tesla," *J. Cardiovasc. Magn. Reson.*, vol. 12, no. 1, p. 67, Nov. 2010.

[33] P. Lanzer, E. H. Botvinick, N. B. Schiller, L. E. Crooks, M. Arakawa, L. Kaufman, P. L. Davis, R. Herfkens, M. J. Lipton, and C. B. Higgins, "Cardiac imaging using gated magnetic resonance.," *Radiology*, vol. 150, no. 1, pp. 121–127, Jan. 1984.

[34] M. E. Crowe, A. C. Larson, Q. Zhang, J. Carr, R. D. White, D. Li, and O. P. Simonetti, "Automated rectilinear self-gated cardiac cine imaging," *Magn. Reson. Med.*, vol. 52, no. 4, pp. 782–788, Oct. 2004.

[35] D. R. Bailes, D. J. Gilderdale, G. M. Bydder, A. G. Collins, and D. N. Firmin, "Respiratory ordered phase encoding (ROPE): a method for reducing respiratory motion artefacts in MR imaging.," *Journal of computer assisted tomography*, vol. 9, no. 4. pp. 835–838, 1985.

[36] X. Hu, T. H. Le, T. Parrish, and P. Erhard, "Retrospective estimation and correction of physiological fluctuation in functional MRI," *Magn. Reson. Med.*, vol. 34, no. 2, pp.

201–212, Aug. 1995.

[37] R. L. Ehman and J. P. Felmlee, "Adaptive technique for high-definition MR imaging of moving structures.," *Radiology*, vol. 173, no. 1, pp. 255–263, Oct. 1989.

[38] P. G. Danias, M. V McConnell, V. C. Khasgiwala, M. L. Chuang, R. R. Edelman, and W. J. Manning, "Prospective navigator correction of image position for coronary MR angiography.," *Radiology*, vol. 203, no. 3, pp. 733–6, Jun. 1997.

[39] E. B. Welch, P. J. Rossman, J. P. Felmlee, and A. Manduca, "Self-navigated motion correction using moments of spatial projections in radial MRI," *Magn. Reson. Med.*, vol. 52, no. 2, pp. 337–345, Aug. 2004.

[40] C. Stehning, P. Börnert, K. Nehrke, H. Eggers, and M. Stuber, "Free-breathing whole-heart coronary MRA with 3D radial SSFP and self-navigated image reconstruction," *Magn. Reson. Med.*, vol. 54, no. 2, pp. 476–480, Aug. 2005.

[41] A. Fischer, A. Menini, A. Bustin, K. M. Johnson, C. J. Francois, and A. C. S. Brau, "Fully self-gated motion compensated cine reconstruction from free-breathing ungated 2D radial cardiac MRI data," in *Proc. Intl. Soc. Mag. Reson. Med.*, 2016, no. 24, p. 0789.

[42] D. P. Hinton, L. L. Wald, J. Pitts, and F. Schmitt, "Comparison of cardiac MRI on 1.5 and 3.0 Tesla clinical whole body systems.," *Invest. Radiol.*, vol. 38, no. 7, pp. 436–42, Jul. 2003.

[43] P. Rajiah and M. A. Bolen, "Cardiovascular MR imaging at 3T: opportunities, challenges, and solutions.," *Radiographics*, vol. 34, no. 6, pp. 1612–35, 2014.

[44] T. Niendorf, D. K. Sodickson, G. A. Krombach, and J. Schulz-Menger, "Toward cardiovascular MRI at 7 T: clinical needs, technical solutions and research promises," *Eur Radiol*, vol. 20, no. 12, pp. 2806–2816, 2010.

[45] S. Gabriel, R. W. Lau, and C. Gabriel, "The dielectric properties of biological tissues: II. Measurements in the frequency range 10 Hz to 20 GHz," *Phys. Med. Biol.*, vol. 41, no. 11, pp. 2251–2269, Nov. 1996.

[46] M. A. Cloos, F. Knoll, T. Zhao, K. T. Block, M. Bruno, G. C. Wiggins, and D. K. Sodickson, "Multiparametric imaging with heterogeneous radiofrequency fields," *Nat.*

Commun., vol. 7, p. 12445, Aug. 2016.

[47] A. Tannús and M. Garwood, "Adiabatic Pulses," *NMR Biomed*, vol. 10, pp. 423–434, 1997.

[48] K. M. Franklin, B. M. Dale, and E. M. Merkle, "Improvement in B1-inhomogeneity artifacts in the abdomen at 3T MR imaging using a radiofrequency cushion," *J. Magn. Reson. Imaging*, vol. 27, no. 6, pp. 1443–1447, Apr. 2008.

[49] J. G. Whisenant, R. D. Dortch, W. Grissom, H. Kang, L. R. Arlinghaus, and T. E. Yankeelov, "Bloch–Siegert B1 Mapping Improves Accuracy and Precision of Longitudinal Relaxation Measurements in the Breast at 3 T," *Tomography*, vol. 2, no. 4, pp. 250–259, Dec. 2016.

[50] E. K. Insko and L. Bolinger, "Mapping of the Radiofrequency Field," *J. Magn. Reson. Ser. A*, vol. 103, no. 1, pp. 82–85, Jun. 1993.

[51] R. Stollberger and P. Wach, "Imaging of the active B$_1$ field in vivo," *Mag. Res. Med.*, vol. 35, no. 2, pp. 246–251, 1996.

[52] C. H. Cunningham, J. M. Pauly, and K. S. Nayak, "Saturated double-angle method for rapid B1+ mapping," *Magn. Reson. Med.*, vol. 55, pp. 1326–1333, 2006.

[53] V. L. Yarnykh, "Actual flip-angle imaging in the pulsed steady state: A method for rapid three-dimensional mapping of the transmitted radiofrequency field," *Magn. Reson. Med.*, vol. 57, no. 1, pp. 192–200, Jan. 2007.

[54] L. I. Sacolick, F. Wiesinger, I. Hancu, and M. W. Vogel, "B1 mapping by Bloch-Siegert shift.," *Magn. Reson. Med.*, vol. 63, no. 5, pp. 1315–22, May 2010.

[55] K. Nehrke and P. Börnert, "DREAM-a novel approach for robust, ultrafast, multislice B1 mapping," *Magn. Reson. Med.*, vol. 68, pp. 1517–1526, 2012.

[56] K. Nehrke, M. J. Versluis, A. Webb, and P. Börnert, "Volumetric B1+ Mapping of the Brain at 7T using DREAM," *Magn. Reson. Med.*, vol. 71, no. 1, pp. 246–256, Jan. 2014.

[57] K. Sung and K. S. Nayak, "Measurement and characterization of RF nonuniformity over the heart at 3T using body coil transmission," *J. Magn. Reson. Imaging*, vol. 27, no. 3, pp. 643–648, Mar. 2008.

[58] H. Clique, H.-L. M. Cheng, P.-Y. Marie, J. Felblinger, and M. Beaumont, "3D

myocardial T1 mapping at 3T using variable flip angle method: Pilot study," *Magn. Reson. Med.*, vol. 71, no. 2, pp. 823–829, Feb. 2014.

[59] M.Livio, *The Golden Ratio: The story of Phi, The Worlds's most astonishing number.* New York.: Broadway Books, 2002.

[60] S. Winkelmann, T. Schaeffter, T. Koehler, H. Eggers, and O. Doessel, "An optimal radial profile order based on the Golden Ratio for time-resolved MRI," *IEEE Trans Med Imaging*, vol. 26, no. 1, pp. 68–76, 2007.

[61] A. Bustin, A. Menini, S. Liu, T. Rincón-Domínguez, D. Burschka, M. A. Janich, S. Wolff, O. Shubayev, D. W. Stanley, F. Odille, and A. C. Brau, "Motion Compensated Reconstruction in Accelerated Single-Shot Cardiac MRI," in *Intl. Soc. Mag. Reson. Med. 23*, 2015, p. 0810.

[62] K. P. Pruessmann, M. Weiger, P. Börnert, and P. Boesiger, "Advances in sensitivity encoding with arbitrary *k* -space trajectories," *Magn. Reson. Med.*, vol. 46, no. 4, pp. 638–651, Oct. 2001.

[63] A. N. Tikhonov, *Numerical Methods for the Solution of Ill-Posed Problems.* Springer, 1995.

[64] D. J. Atkinson and R. R. Edelman, "Cineangiography of the heart in a single breath hold with a segmented turboFLASH sequence.," *Radiology*, vol. 178, no. 2, pp. 357–360, 1991.

[65] C. B. Paschal and H. D. Morris, "K-space in the clinic," *J. Magn. Reson. Imaging*, vol. 19, no. 2, pp. 145–159, Feb. 2004.

[66] J. G. Pipe, "Motion correction with PROPELLER MRI: Application to head motion and free-breathing cardiac imaging," *Magn. Reson. Med.*, vol. 42, no. 5, pp. 963–969, Nov. 1999.

[67] E. Candès and J. Romberg, "Sparsity and incoherence in compressive sampling," *Inverse Probl.*, vol. 23, no. 3, pp. 969–985, Jun. 2007.

[68] D. L. Donoho, "Compressed sensing," *IEEE Trans. Inf. Theory*, vol. 52, no. March 2008, pp. 1289–1306, 2006.

[69] M. Lustig, D. L. Donoho, J. M. Santos, and J. M. Pauly, "Compressed Sensing MRI,"

IEEE Signal Process. Mag., vol. 25, no. 2, pp. 72–82, Mar. 2008.

[70] E. J. Candes, J. Romberg, and T. Tao, "Robust uncertainty principles: exact signal reconstruction from highly incomplete frequency information," *IEEE Trans. Inf. Theory*, vol. 52, no. 2, pp. 489–509, Feb. 2006.

[71] S. M. Shea, R. M. Kroeker, V. Deshpande, G. Laub, J. Zheng, J. P. Finn, and D. Li, "Coronary artery imaging: 3D segmented k-space data acquisition with multiple breath-holds and real-time slab following," *J. Magn. Reson. Imaging*, vol. 13, no. 2, pp. 301–307, Feb. 2001.

[72] M. Saranathan, M. M. Khalighi, G. H. Glover, P. Pandit, and B. K. Rutt, "Efficient Bloch-Siegert B1+ mapping using spiral and echo-planar readouts.," *Magn. Reson. Med.*, vol. 70, no. 6, pp. 1669–73, Dec. 2013.

[73] R. A. Lerski and J. D. de Certaines, "Performance assessment and quality control in MRI by Eurospin test objects and protocols.," *Magn. Reson. Imaging*, vol. 11, no. 6, pp. 817–33, 1993.

[74] W. M. Brink, P. Börnert, K. Nehrke, and A. G. Webb, "Ventricular B 1 + perturbation at 7 T - real effect or measurement artifact?," *NMR Biomed.*, vol. 27, no. 6, pp. 617–620, Jun. 2014.

[75] K. Nehrke, A. M. Sprinkart, and P. Börnert, "An in vivo comparison of the DREAM sequence with current RF shim technology," *Magn. Reson. Mater. Physics, Biol. Med.*, vol. 28, no. 2, pp. 185–194, Apr. 2015.

[76] M. Schär, H. Ding, and D. A. Herzka, "Improvement in B1+ Homogeneity and Average Flip Angle Using Dual-Source Parallel RF Excitation for Cardiac MRI in Swine Hearts," *PLoS One*, vol. 10, no. 10, p. e0139859, Oct. 2015.

[77] S. E. Fischer, M. Stuber, M. B. Scheidegger, and P. Boesiger, "Limitations of stimulated echo acquisition mode (steam) techniques in cardiac applications," *Magn. Reson. Med.*, vol. 34, no. 1, pp. 80–91, Jul. 1995.

[78] A. Sbrizzi, H. Hoogduin, J. J. Lagendijk, P. Luijten, and C. A. T. van den Berg, "Robust reconstruction of B1+ maps by projection into a spherical functions space," *Magn. Reson. Med.*, vol. 71, no. 1, pp. 394–401, Jan. 2014.

[79] O. Weinberger, L. Winter, M. A. Dieringer, A. Els, C. Oezerdem, J. Rieger, A. Kuehne, A. M. Cassara, H. Pfeiffer, F. Wetterling, and T. Niendorf, "Local Multi-Channel RF Surface Coil versus Body RF Coil Transmission for Cardiac Magnetic Resonance at 3 Tesla: Which Configuration Is Winning the Game?," *PLoS One*, vol. 11, no. 9, p. e0161863, Sep. 2016.

[80] W. Grissom, C. Yip, Z. Zhang, V. A. Stenger, J. A. Fessler, and D. C. Noll, "Spatial domain method for the design of RF pulses in multicoil parallel excitation," *Magn. Reson. Med.*, vol. 56, no. 3, pp. 620–629, Sep. 2006.

[81] S. J. Malik, D. J. Larkman, D. P. O'Regan, and J. V. Hajnal, "Subject-specific water-selective imaging using parallel transmission," *Magn. Reson. Med.*, vol. 63, no. 4, pp. 988–997, Apr. 2010.

[82] W. T. Clarke, M. D. Robson, and C. T. Rodgers, "Bloch-Siegert B1+-mapping for human cardiac 31 P-MRS at 7 Tesla," *Magn. Reson. Med.*, vol. 76, no. 4, pp. 1047–1058, Oct. 2016.

[83] X. Zhang and B. He, "Imaging electric properties of human brain tissues by B1 mapping: A simulation study," *J. Phys. Conf. Ser.*, vol. 224, no. 1, p. 012077, Apr. 2010.

[84] U. Katscher, T. Voigt, C. Findeklee, P. Vernickel, K. Nehrke, and O. Dossel, "Determination of Electric Conductivity and Local SAR Via B1 Mapping," *IEEE Trans. Med. Imaging*, vol. 28, no. 9, pp. 1365–1374, Sep. 2009.

[85] T. Rincón-Domínguez, A. Menini, A. Bustin, A. B. Solana, M. A. Janich, G. Kudielka, D. Burschka, and A. C. Brau, "Multiple accelerated single shot acquisition for motion correction in MRI. ESMRMB 2015, 32nd Annual Scientific Meeting, Edinburgh, UK, 1-3 October: Abstracts, Thursday," in *Magnetic Resonance Materials in Physics, Biology and Medicine*, 2015, vol. 28, no. 42, pp. 1–135.